TECHNICAL NOTES 9

FLOTATION

Flotation is the most widely used mineral separation method. It is the preferred method of mineral recovery for many of the most important minerals that are recovered and large tonnages of ore are processed by flotation annually.

The underlying principles of the flotation process are well established but it has proved to be unusually difficult to build quantitative predictive models that can be used to simulate the operation of flotation cells in typical industrial circuits. The reason for the difficulty lies in the complexity of the many micro processes that combine to produce the overall result which is the separation of different mineral species by virtue of the differential surface conditions that can be induced on the various minerals. In the flotation cell an agitated slurry is aerated by introducing a cloud of air bubbles that are typically about a millimeter in size. The agitation of the slurry is sufficient to keep the solid particles in suspension although the suspension is usually not uniform with the larger heavier particles tending to remain in the lower parts of the cell.

The rising bubbles can and do collide with the suspended solid particles and those particles that have appropriate surface characteristics can attach to a rising bubbles and can therefore be carried upward eventually reaching the surface of the slurry. Each bubble will have many encounters with particles during its rise through the slurry and a bubble can carry several particles to the top of the slurry.

A more or less stable layer of froth is maintained on the surface of the slurry. Particles that are attached to bubbles will tend to remain attached at air-water interfaces when the bubble enters the froth layer. Particles that are retained in the froth are recovered at the lip of the froth weir at the edge of the flotation cell. The recovery of the froth is accomplished by the natural mobility of the froth which causes it to flow over the weir and the recovery is sometimes assisted by mechanical paddles.

Within this general macroscopic view of the flotation process as a whole, several distinct micro processes can be identified. Each of these plays a role in determining how individual solid particles will respond while they are in a flotation cell. Prior to any flotation taking place, a number of detailed chemical processes occur on and exceedingly close to the surfaces of the particles. This is a chemical conditioning step and it is necessary in order to ensure that differential hydrophobicity is achieved with respect to the different mineral species that are present. Minerals that have strongly hydrophobic surfaces have a greater chance of recovery into the froth phase than particles that are weakly hydrophobic or hydrophilic. The chemical conditioning of mineral surfaces for flotation has been the subject of sustained research efforts for the best part of a century and a great deal is known about the surface chemistry and the role the chemical factors play in the aqueous phase and on the particle surfaces. However most of this understanding is qualitative with comparatively little information emerging that allows quantitative prediction of such important variables as contact angle and other measures of hydrophobicity. As a result, quantitative models of flotation cell performance do not at present make any significant use of quantitative chemical parameters such as for example

the pH of the slurry and the concentration of chemical collectors or frothers to define overall process behavior. Hopefully the situation will change in the future and an understanding of the surface chemistry will play its appropriate role in the development of truly predictive quantitative models for flotation.

Much the same can be said for the froth phase. Although a great deal is known about the structure of froths and foams, it is not possible to make quantitative predictions about froth stability and froth mobility and their effect on the ability to hold and ultimately recover mineral particles that enter the froth attached to bubbles.

When formulating a quantitative model for the flotation process, it is necessary to start from the premise that, by virtue of appropriate chemical conditioning of the slurry, minerals will exhibit varying levels of surface hydrophobicity and, consequently, a separation of particles is possible based on the proportion of different mineral exposure on the surface. Likewise it is presumed that a more or less stable and mobile layer of froth will persist on the surface of the slurry which will gather and recover a proportion of the adhering mineral particles.

8.1 A Kinetic Approach to Flotation Modeling

Almost all successful models of the flotation process have been based on the premise that flotation is a kinetic process. In this way a model can be formulated in terms of a rate of flotation which can be quantified in terms of some of the many chemical and physical factors that define the environment inside a flotation cell. The formulation of a suitable rate model is not straightforward and it must be based on an analysis of the individual sub processes that affect an individual particle in the

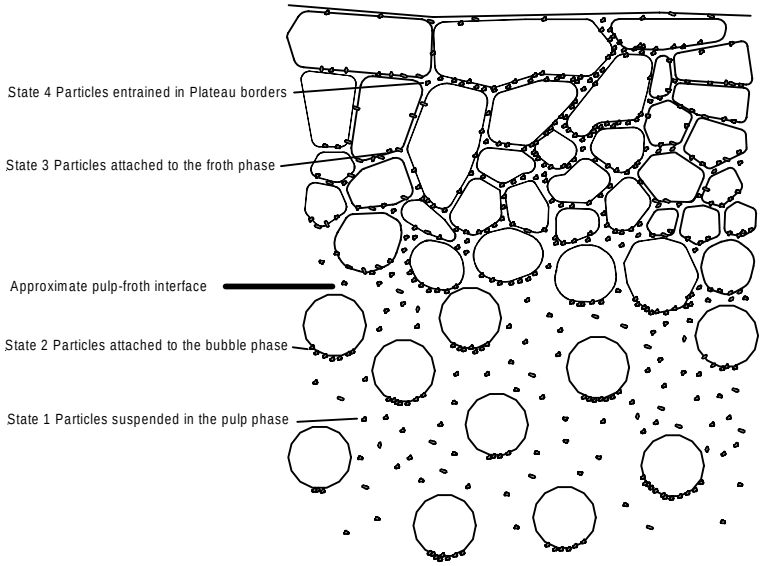

Figure 9.1 *Four states in which particles exist in a flotation cell.*

flotation environment. These sub processes can be identified by noting that a particle must successfully complete the following steps in order to be recovered in the froth phase of a flotation cell.

1. Each particle must achieve a level of hydrophobicity that will permit it to attach to a rising bubble.
2. The particle must be suspended in the pulp phase of the cell.
3. The particle must collide with a rising bubble.
4. The particle must adhere to the bubble.
5. The particle must not detach from the bubble during passage through the pulp phase.
6. The particle must not detach from the bubble as the bubble leaves the pulp phase and enters the froth phase.
7. The particle must not detach and drain from the froth during the passage of the froth to the weir.

In order to incorporate these sub processes into a useful kinetic model it is necessary to consider the pulp phase and the froth phase separately because the kinetic processes that occur are different in each. The particles are considered to be in one of four possible states in the flotation cell. These states are illustrated in Figure 9.1. The four states are: suspension in the pulp phase, attached to the bubble phase, attached to the air-water interface in the froth phase and suspended in the Plateau borders of the froth phase.

8.1.1 Pulp phase

The pulp phase is aerated so that bubbles are formed continuously and rise through the pulp as an upward moving cloud. The solid particles are suspended throughout the pulp by the circulation that is induced by the agitator. At any point in the pulp the bubbles are moving upward relative to the pulp at their local rise velocity and the particles are moving downward at their local settling velocity. This does not mean that the bubbles are traveling vertically upward and the particles vertically downward because there is considerable lateral and vertical motion of the liquid which is necessary to keep the particles suspended in the pulp. Nevertheless it is this relative velocity between particles and bubbles that is primarily responsible for collisions between particles and bubbles.

Particles can leave the pulp phase through one of two routes: by collision with and attachment to a bubble or direct to the froth phase by entrainment at the pulp-froth interface. The collision and attachment sub-processes are discussed in some detail later in this chapter and they govern, to a large extent, the kinetic behavior of the particles in a flotation cell.

Particles can re-enter the pulp phase by detachment from a bubble or by draining from the Plateau borders in the froth.

8.1.2 Bubble phase

The bubble phase consists of a cloud of bubbles that rise through the pulp phase. A particle transfers from the pulp phase to the bubble phase by a process of bubble-particle collision and particle

attachment. Once a particle is attached to a bubble it moves with the bubble and eventually it will reach the froth phase unless it is detached from the bubble in which case it returns to the pulp phase. Bubbles become steadily more and more heavily loaded with attached particles as the bubble passes through the pulp.

8.1.3 Froth phase

Particles enter the froth phase when a bubble carrying the particles crosses the pulp-froth interface. The froth phase floats on top of the pulp phase and is formed by the bubbles that break through the surface of the pulp phase. The water in the flotation cell is conditioned to promote the formation of a more or less stable froth. The bubbles do not burst when they cross the interface and each one carries a skin of water into the froth phase. The bubbles move close together with a single film of liquid separating the individual bubbles. When the bubbles are small, these boundary films are curved. The liquid drains from the films which become thinner and eventually break causing adjacent bubbles to coalesce. The bubbles become larger and larger and polyhedral in shape. At the junction of the polyhedral edges of the bubbles, Plateau borders form which act as a network of more or less tubular conduits through which the draining liquid can move downward. The particles that remain attached to the surface of bubbles in the froth move with the froth until they are eventually recovered in the concentrate froth when it passes over the froth lip of the flotation cell. Particles can become detached from the liquid film and transfer from the froth phase to the Plateau borders in the froth from where they can drain back into the pulp phase.

8.1.4 Entrained phase

Particles are entrained in the Plateau borders of the froth and will tend to settle down toward the pulp-froth interface under the influence of gravity. This settling is assisted further by the draining of the water as the films between bubbles in the froth become thinner and possibly break. This water flows through the network of Plateau borders and eventually re-enters the pulp phase. Particles enter the entrained phase by detachment from the air-water surfaces in the froth and also by direct entrainment from the pulp phase immediately below the pulp-froth interface on the top of the pulp.

8.2 A Kinetic Model for Flotation

The kinetic model for flotation is based on the following simple principle. A single bubble rising upward through the pulp phase will collide with suspended particles and some of these particles will attach to the bubble surface and will travel upward with the bubble. The rate at which bubbles collide with particles depends on the size of the bubbles and the size of the particles, their relative velocities, and the concentration of particles in the pulp. The number of particles that can collide with the bubble can be calculated in the following way.

The volume of pulp that is swept by a bubble per second is $\frac{\pi}{4}D_{bh}^2 U_b$ where U_b is the local rise velocity of the bubble and D_{bh} the bubble diameter projected on to the horizontal plane. This is generally different to the volume equivalent bubble diameter D_{be} because a rising bubble distorts into an ellipsoidal shape unless it is very small.

A population balance approach is taken so that the population of particles in the cell is conceptually divided into classes so that particles in any one class are all similar in size and composition. The number of potential collisions with the particles of type *ij* is proportional to the concentration C_{ij} of these particles in the pulp phase. The diameter of the swept volume from which a particle of size d_{pi} may be captured is $D_{bh} + d_{pi}$. The number of potential collisions with particles of size d_{pi} is given by

$$\text{Number of potential collisions with particles of type } ij = \frac{\pi}{4}(D_{bh} + d_{pi})^2(U_b + v_{Tij})C_{ij} \quad (9.1)$$

where U_b is the velocity of rise of the bubble and v_{Ti} is the free fall velocity of the particle. These are taken to be the terminal velocities in the gravitational field in both cases although, in the turbulent circulating flow inside a flotation cell, terminal velocities may not be achieved by all particles and bubbles.

The rate of transfer of particles from the pulp phase to the bubble phase (transitions from state 1 to state 2 in Figure 9.1) is given by

Ideal rate of transfer = number of potential collisions × number of bubbles/unit volume

$$= \frac{\pi}{4}(D_{bh} + d_{pi})^2(U_b + v_{Tij})C_{ij} \times \frac{G_v \tau_b}{\frac{\pi}{6}D_{be}^3} \quad \text{kg/m}^3 \text{ of cell volume} \quad (9.2)$$

where G_v is the specific aeration rate in m^3 air/s m^3 cell volume and τ_b is the average bubble residence time in the cell. D_{be} is the effective spherical diameter of the bubble.

In a real flotation cell, this ideal rate of transfer is never achieved because not all of the potential collisions actually occur and, of those that do occur, not all are successful in achieving adhesion between the bubble and the particle. The ideal rate is accordingly modified to reflect these inefficiencies

$$\text{Rate of transfer} = \frac{3}{2}(D_{be} + d_{pi})^2(U_b + v_{Tij})C_{ij} \times \frac{G_v \tau_b}{D_{be}^3} \times E_{Cij}E_{Aij}(1 - E_{Dij}) \text{ kg/m}^3 \text{ of cell} \quad (9.3)$$

where E_{Cij} is the fraction of particles that are in the path of the bubble which actually collide with it. E_{Aij} is the fraction of bubble-particle collisions that lead to successful attachment.

E_{Dij} is the fraction of particles of type *ij* that are detached from the bubble during the time that it takes the bubble to rise through the pulp phase. The development of a quantitative kinetic model for the flotation process starts with models for E_{Cij}, E_{Aij}, and E_{Dij}.

The sub processes of collision, attachment and detachment can be considered to be independent since they are governed by essentially different forces. The collision process is dominated by the local hydrodynamic conditions around the bubble. The attachment process is dominated by the short-

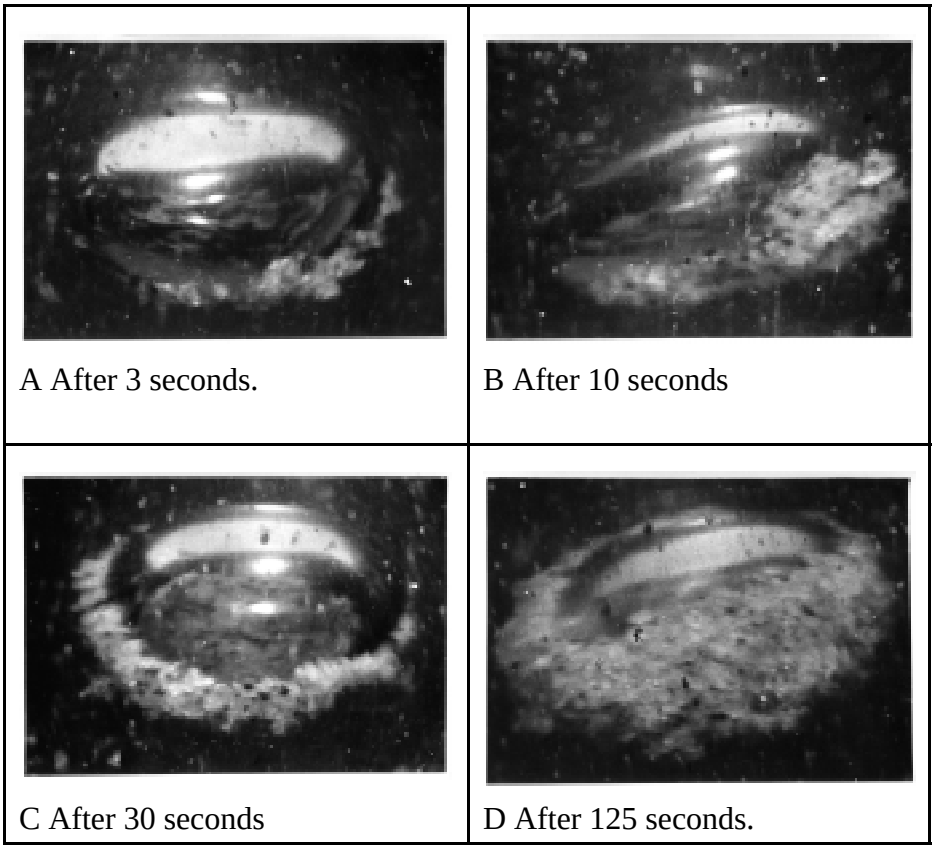

Figure 9.2 *Loading of a single bubble during flotation.*

range surface forces and by the drainage and rupture characteristics of the thin liquid film between the bubbles and contacting particles. The detachment process is governed by stability considerations of the-multi particle aggregates that are formed on the bubble surface following successful attachment of the particles. These processes are largely independent of each other and, as will be shown below, require different models for their quantitative description.

The efficiency of bubble capture is reduced by the presence of other adhering particles which cover a portion of the bubble surface area. A necessary result of this kinetic model is that any bubble will

become progressively covered with attached particles during its passage through the pulp phase. This behavior has been confirmed by direct experimental observation and is clearly shown in the photographic sequence in Figure 9.2. These photographs of a single bubble were taken to record the increasing load of particles during the lifetime of the bubble in the pulp. The essential elements of the collection of particles by bubbles are clearly illustrated in these photographs. The sweeping action of the fluid motion which makes the particles slide over the bubble and accumulate on the lower surface is strikingly evident. This behavior influences both the collision efficiency E_c and the adhesion efficiency E_A.

8.2.1 Particle-bubble collisions

Not every particle in the path of a rising bubble will collide with the bubble because, as the bubble advances through the water, it forces the water aside and this tends to carry the particles out of the path of and around the bubble. The processes that are at work can be seen in Figure 9.3 which shows the streamlines that are formed around a bubble as it advances through the pulp. The streamlines shown in Figure 9.3 were calculated for two extreme flow regimes: Stokes flow which applies when the bubble Reynolds number is very much less than unity and potential flow which applies when the bubble Reynolds number is very much larger than unity. The streamlines show the trajectories that a small neutrally buoyant particle will take during the encounter with the bubbles. Such a particle will collide with the bubble only if it is on a streamline that has it closest approach to the bubble less than or equal to the radius of the particle. The streamlines shown in Figure 9.3 were calculated so that they are uniformly distributed a long way in front of the bubble. This means the two sets of streamlines are directly comparable and it is easy to see that the choice of flow model will have a significant effect on the value of E_c. Potential flow leads to much higher collision efficiencies than Stokes flow.

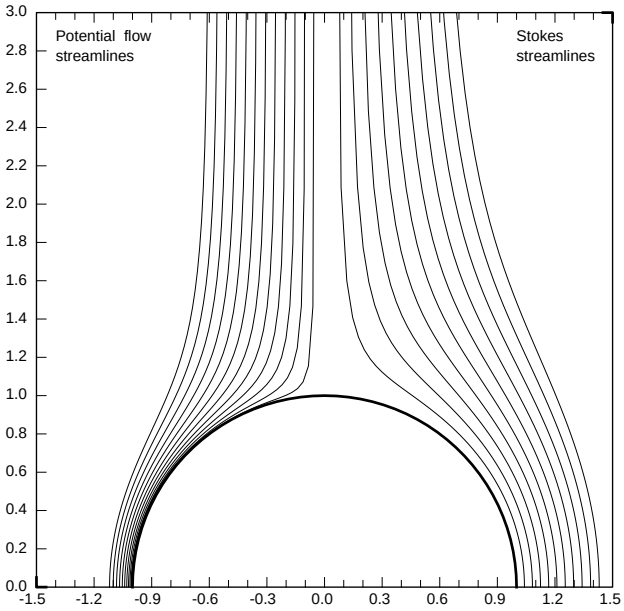

Figure 9.3 *Streamlines for water around a rigid spherical bubble calculated assuming potential flow (left-hand side) and Stokes flow (right-hand side)*

It can be seen from Figure 9.3 that a neutrally buoyant particle of diameter $d_p = 0.1\ D_b$ must be no more than about 17% of a bubble radius off the center line of the collision path if it is to make contact with the bubble surface during the flypast under Stokes flow. On the other hand a neutrally buoyant particle of the same size would touch the bubble surface if it were as far out as 56% of the bubble radius under potential flow conditions. Obviously the collision efficiency E_c for particles of this kind is quite small in either case but is significantly lower for Stokes flow

conditions. This agrees with intuition since a faster moving bubble will sweep up particles in its path more effectively than a slow moving bubble.

The streamlines plotted in Figure 9.3 result from the analytical solutions of the continuity equations around solid spheres moving through Newtonian fluids. These solutions can be applied to the motion of a bubble through water provided that the surface of the bubble can be assumed to be immobile. This is usually assumed when analyzing flotation processes because of the relatively large quantities of surfactant that are available to concentrate at the bubble surface. These mathematical solutions under Stokes and potential flow conditions can be found in standard texts on fluid mechanics.

The streamlines are governed by the following equations.

$$\Psi = \frac{\psi}{U_b R_b^2} = \sin^2\theta\left(\frac{1}{2}\left(\frac{r}{R_b}\right)^2 - \frac{3}{4}\frac{r}{R_b} + \frac{R_b}{4r}\right) = \sin^2\theta\,\mathscr{F}_{St}(r) \tag{9.4}$$

for Stokes flow and

$$\Psi = \frac{\psi}{U_b R_b^2} = \sin^2\theta\left(\frac{1}{2}\left(\frac{r}{R_b}\right)^2 - \frac{R_b}{2r}\right) = \sin^2\theta\,\mathscr{F}_{Pot}(r) \tag{9.5}$$

for potential flow. r and θ are the spherical spatial coordinates with the bubble center as origin. U_b is the velocity of rise of the bubble and R_b is the radius of the bubble.

Neither of the two extreme flow regimes, Stokes or potential flow, will be applicable under all conditions in operating flotation cells and a model is required that will hold for all values of the bubble Reynolds from low (Stokes regime) to high (potential flow). Using published streamline patterns for rigid spheres moving in fluids over a range of bubble Reynolds numbers as a guide, Yoon and Luttrell used a weighted sum of the Stokes and potential flow solutions to describe the streamlines around a sphere at Reynolds numbers in the range from 0 to 100.

$$\Psi = \sin^2\theta\left(\alpha\mathscr{F}_{st}(r) + (1-\alpha)\mathscr{F}_{Pot}(r)\right) = \sin^2\theta\,\mathscr{F}(r) \tag{9.6}$$

with $\mathscr{F}(r)$ given by

$$\mathscr{F}(r) = \frac{1}{2}\left(\frac{r}{R_b}\right)^2 - \frac{3}{4}\alpha\frac{r}{R_b} + \left(\frac{3}{4}\alpha - \frac{1}{2}\right)\frac{R_b}{r} \tag{9.7}$$

α is a dimensionless parameter that depends on the bubble Reynolds number and has the value 1 when $Re_b = 0$ (Stokes regime) and asymptotes to the value 0 at high Re_b (potential flow). α also depends on the value of r. For values of r only slightly larger than R_b, α is close to unity.

α is related to the bubble Reynolds number by

$$\alpha = \exp\left(-\frac{4Re_b^{0.72}}{45} \frac{r_p'}{1 + r_p'} \right) \tag{9.8}$$

where $r_p' = \frac{R_p}{R_b}$ and R_p is the radius of the particle.

The bubble Reynolds number $Re_b = \frac{D_b U_b \rho_w}{\mu_w}$ can be calculated from the terminal rise velocity given the bubble size and the load of solids that it carries (see Section 9.5).

8.2.2 A model for collision efficiencies

The collision efficiency is calculated as the fraction of the particles which are in the path of the bubble that actually collide with the bubble. In order to find which particles collide with the bubble, it is helpful to establish the stream lines for the particle motion since particles will deviate from the fluid streamlines that are shown in Figure 9.3. Particles deviate from the fluid streamlines because they fall relative to the fluid as a result of their greater density and because inertia prevents the particle from accelerating at the same rate as the fluid when the fluid deviates from a straight line path as it approaches a bubble.

The radial and azimuthal components of the fluid velocity are given by

$$u_r = -\frac{1}{r^2 \sin\theta} \frac{\partial \psi}{\partial \theta} = -2 \frac{U_b R_b^2}{r^2} \cos\theta \mathscr{F}(r) \tag{9.9}$$

$$u_\theta = \frac{1}{r \sin\theta} \frac{\partial \psi}{\partial r} = \frac{U_b R_b^2}{r} \sin\theta \mathscr{F}'(r) \tag{9.10}$$

If the inertia of the particles is neglected, the particles move relative to the fluid at their terminal settling velocities, v_T. Terminal settling velocities can be calculated using the method described in Section 4.4.1. Then the components of the particle velocity vector are given by

$$v_r = u_r - v_T \cos\theta \tag{9.11}$$

and

$$v_\theta = u_\theta + v_T \sin\theta \tag{9.12}$$

The stream function for the particle motion is therefore

$$\psi_p = U_b R_b^2 \sin^2\theta \left(\mathscr{F}(r) + \frac{1}{2} \frac{v_T}{U_b} \left(\frac{r}{R_b} \right)^2 \right) \tag{9.13}$$

The streamlines for water calculated using equation 9.6 and the trajectories of particles having

terminal settling velocity equal to $0.1U_b$, calculated using equation 9.13, are shown in Figure 9.4 for a bubble rising with a Reynolds number of 20.

The collision efficiency for particles of type *ij* is calculated as the flux of particles crossing an imaginary hemisphere of radius $R_b + R_p$ that shrouds the front hemisphere of the bubble divided by the flux of particles that cross a horizontal plane of area $\pi(R_b + R_p)^2$.

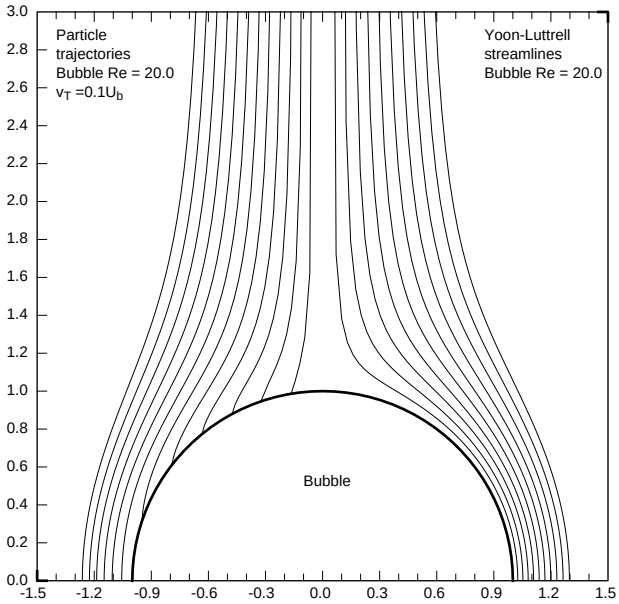

Figure 9.4 *Streamlines for water (right-hand side) calculated using equation 9.6 and streamlines for particles (left-hand side)having terminal settling velocity equal to $0.1U_b$ calculated using equation 9.13*

Therefore

$$E_{Cij} = \frac{-2\pi \int_0^{\frac{\pi}{2}} v_r\big|_{r=R_b+R_p} (R_b + R_p)\sin\theta\,(R_b + R_p)\,d\theta}{\pi(R_b + R_p)^2(U_b + v_{Tij})} = \frac{\dfrac{2U_b R_b^2 \mathscr{F}(R_b+R_p)}{(R_b + R_p)^2} + v_{Tij}}{U_b + v_{Tij}} \qquad (9.14)$$

Collision efficiencies can be measured in the laboratory using single bubble flotation experiments

with particles that are conditioned to be extremely hydrophobic. These particles have adhesion efficiencies of 1.0 and the measured collection efficiency is therefore equal to the collision efficiency. The collision efficiencies predicted by equation 9.14 are compared to experimental data in Figure 9.5. The data of Afruns and Kitchener were determined using quartz particles and that of Yoon and Luttrell using coal particles. The predicted efficiencies are close to the measured data confirming that the theory provides a reasonable model of the collision process although it over estimates the collision efficiency by a factor of about 2 for bubbles approaching 1 mm in diameter.

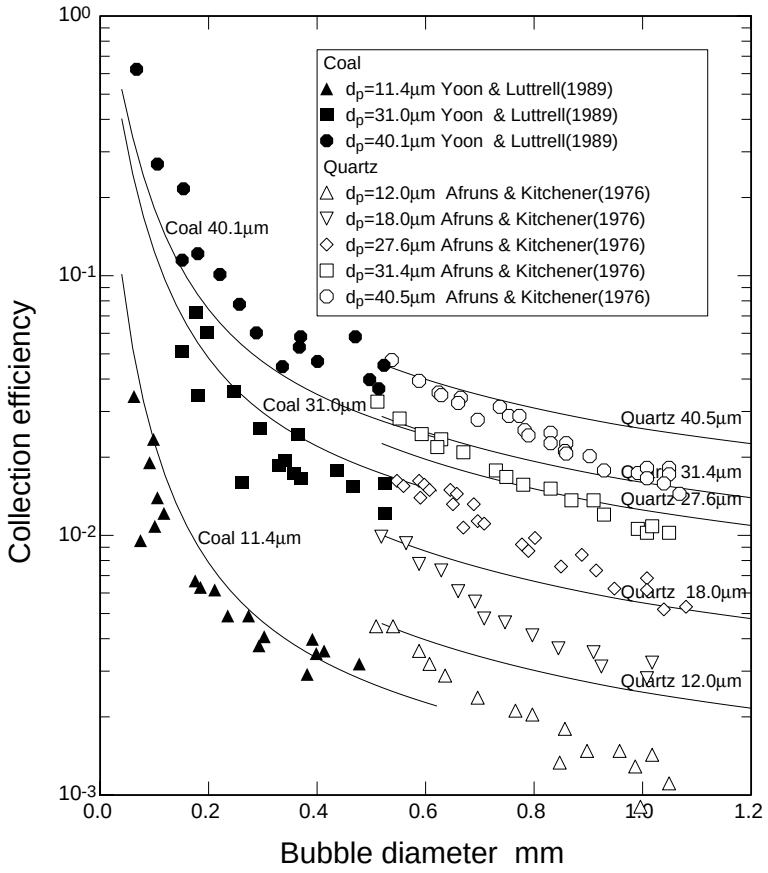

Figure 9.5 *Comparison between measured and predicted collection efficiencies. The lines were calculated using equation 9.14 for each of the two minerals.*

Another important factor to note is that particles which do strike the bubble will do so at different latitudes on the bubble. This has important implications for the modeling of the attachment process which is discussed in section 9.2.2. The latitude angle at which the particle on streamline Ψ_0 strikes the bubble can be calculated using equation 9.13 by setting $r = R_b + R_p$ and is given by

$$\theta_c = \arcsin\left(\left(\frac{\Psi_0}{\mathscr{F}(R_b+R_p) + \frac{1}{2}\frac{v_T}{U_b}\left(\frac{R_b+R_p}{R_b}\right)^2}\right)^{\frac{1}{2}}\right) \tag{9.15}$$

Particles of type *ij* can start their approach to a bubble at any distance R_o from the collision center line. Each particle of type *ij* will have a maximum distance R_{0ij} from the center line that will result in a grazing trajectory. Providing that $R_o < R_{oij}$ a collision will occur. The collision angle will vary with R_o and since the location of each particle in the pulp is random, θ_c should be regarded as a random variable. Its associated probability distribution can be evaluated by noting that R_o is uniformly distributed in [0, R_{oij}].

R_o can be related to ψ_{po} by noting that far out from the bubble

$$\sin\theta = \frac{R_o}{r} \tag{9.16}$$

so that equation 9.13 gives

$$R_o = \left(\frac{2\psi_{po}}{U_b + v_{Tij}}\right)^{\frac{1}{2}} \tag{9.17}$$

and

$$R_{oij} = \left(\frac{2\psi_{poij}}{U_b + v_{Tij}}\right)^{\frac{1}{2}} \tag{9.18}$$

where ψ_{poij} is the value of the particle stream function for the streamline that represents the grazing trajectory for a particle of type *ij* at the equator of the bubble. This is evaluated using equation 9.13 with $\theta = \pi/2$ and $r = R_b + R_{pij}$

$$\Psi_{oij} = \mathscr{F}(R_b+R_{pij}) + \frac{1}{2}\frac{v_{Tij}}{U_b}\left(\frac{R_b+R_{pij}}{R_b}\right)^2 \tag{9.19}$$

Substitution of equations 9.17, 9.18 and 9.19 into equation 9.15 gives a simple relationship between θ_c and R_o.

$$\sin\theta_c = \frac{R_o}{R_{oij}} \tag{9.20}$$

By noting the uniform probability distribution of the random variable R_o, the distribution density for the collision angle θ_c is

$$f_{\theta_c}(\theta_c) = \cos\theta_c \tag{9.21}$$

The corresponding cumulative distribution function for θ_c is

$$F_{\theta_c}(\theta_c) = \sin\theta_c \qquad \text{for } 0 \le \theta_c \le \frac{\pi}{2} \tag{9.22}$$

8.2.3 Particle-bubble attachment

The attachment process requires significantly more complex modeling than the collision process which, as shown in the previous section, is governed primarily by the fluid dynamics close to the bubble. The attachment process is governed by hydrodynamic and chemical factors which interact in complex ways that ultimately determine whether a particle will attach to the bubble or not.

When a particle collides with the bubble, the particle cannot immediately attach to the bubble because a thin film of liquid between the particle and the bubble must first drain. When the intervening film becomes sufficiently thin it can rupture allowing the particle to penetrate the skin of the bubble. The three phase contact line that defines the penetration boundary of the bubble around the particle must then develop to a stable configuration that is governed primarily by the contact angle (both receding and advancing) of the solid and also by its shape. Although the actual rupture step is very rapid the film thinning and movement of the three phase contact line are governed by kinetic processes and each requires a finite time. The time taken from the instant of collision to the establishment of a stable three-phase contact is called the induction time which will be represented by t_{ind}. The induction time for a particle is determined primarily by its contact angle but the particle size and shape are also important. Other chemical factors such as the concentration of surfactants at the bubble surface and the interaction between collector adsorbed on the solid and frother on the bubble surface also play a role. Purely physical factors such as the precise orientation of the particle on first contact and the velocity profile close to the bubble surface and surrounding bubble all contribute to this enormously complex phenomenon. A detailed understanding of these effects has not yet been developed to the stage where induction times for irregular particles with heterogenous surfaces can be confidently calculated. However, in general, particles with larger contact angles have shorter induction times than similar particles having smaller contact angles. This variation in induction time is the origin of the differential behavior of particles during flotation and consequently it must form the kernel of any quantitative model of flotation.

While the film thinning, film rupture and receding three-phase contact line are proceeding another, purely physical, process is occurring. The particle is being carried downward over the surface of the bubble by the water as it moves past the bubble surface. Particles against or attached to the bubble are washed to the rear of the bubble. If a stable three-phase contact has been established before the fluid stream lines start to diverge from the bubble, successful attachment is achieved and the particle remains attached to the bubble and continues its journey over the bubble surface until it collides with other particles already attached to the bubble which covers its lower pole. The accumulating collection of particles on the lower surface gradually builds up until the whole of the lower hemisphere of the bubble is covered with adhering particles.

Particles that have not formed a stable three-phase contact by the time the streamlines start to diverge from the bubble surface at the equator are pulled away from the bubble surface and they do not attach. The time taken by a particle to slide over the bubble surface from its point of collision to the point of divergence is called the sliding time, t_s. The fundamental principle that governs the collision model of flotation is that a particle if size d_p and composition g will attach to a bubble of size D_b only if it experiences a successful collision and its induction time is less than the sliding time.

$$t_{ind} \leq t_s \tag{9.23}$$

This should properly be referred to as the Sutherland principle in recognition of his pioneering attempt to put the understanding of flotation principles on a firm scientific basis. This model of the flotation process is illustrated in Figure 9.6

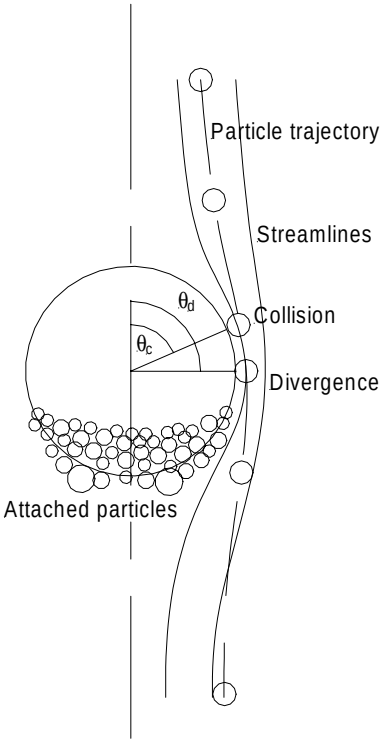

Figure 9.6 *Collision and divergence angle for collisions.*

In order to use the principle embodied in equation 9.23 to calculate the rate at which particles are captured by bubbles, it is necessary to calculate the sliding time and the induction time.

The sliding time for the particle can be calculated with reasonable accuracy from a knowledge of the hydrodynamics in the water close to the bubble surface. The tangential velocity in the water surrounding the bubble can be calculated using the stream function given in equation 9.6

$$u_\theta = \frac{1}{R_b \sin(\theta + \theta_p)} \frac{d\psi}{dr} = U_b \sin(\theta + \theta_p)\left(\frac{r}{R_b} - \frac{3}{4}\alpha + \frac{R_b^2}{2r^2} - \frac{3}{4}\frac{\alpha R_b^2}{r^2} \right) \tag{9.24}$$

where θ_p is the angle subtended at the bubble center by the radius of a particle that touches the bubble. The particle slides over the surface of the sphere approximately at the water velocity at one particle radius from the surface of the bubble which for small particles is given by

$$\begin{aligned} u_\theta &= U_b \sin(\theta + \theta_p)\left[\frac{3}{2}(1 - \alpha + \alpha r_p') + (\frac{1}{2} - \frac{3}{4}\alpha) r_p'^2 \right] \\ &= U_b^* \sin(\theta + \theta_p) \end{aligned} \tag{9.25}$$

where

$$
\begin{aligned}
r_p' &= \frac{R_p}{R_b} \\
U_b^* &= U_b\left[\frac{3}{2}(1-\alpha+\alpha r_p') + (\frac{1}{2}-\frac{3}{4}\alpha)r_p'^2\right]
\end{aligned}
\tag{9.26}
$$

In addition the particle moves relative to the water at its terminal settling velocity so that the sliding time is

$$
\begin{aligned}
t_s &= \int_{\theta_c}^{\frac{\pi}{2}} \frac{R_b + R_b}{u_\theta + v_t \sin(\theta + \theta_p)} d\theta \\
&= \frac{R_b + R_p}{U_b^* + v_t} \int_{\theta_c}^{\frac{\pi}{2}} \frac{d\theta}{\sin(\theta + \theta_p)} \\
&= \frac{R_b + R_p}{2(U_b^* + v_t)} \ln\left[\frac{1-\cos(\frac{\pi}{2}+\theta_p)}{1+\cos(\frac{\pi}{2}+\theta_p)} \times \frac{1+\cos(\theta_c+\theta_p)}{1-\cos(\theta_c+\theta_p)}\right]
\end{aligned}
\tag{9.27}
$$

The maximum sliding time for a particle of size R_p is evaluated from equation 9.27 at $\theta_c = 0$ and is given by

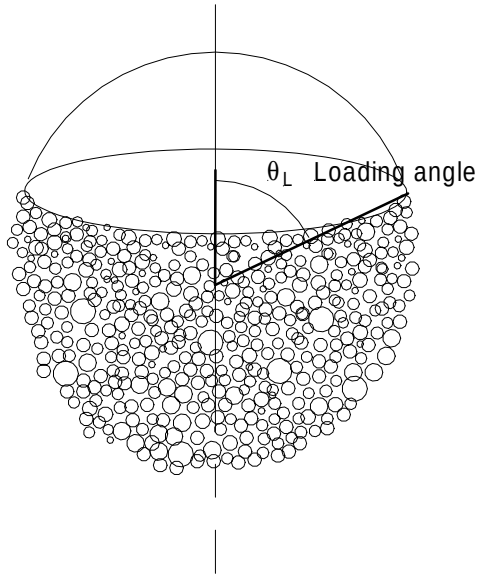

Figure 9.7 *Heavily loaded bubble showing the loading angle.*

$$t_{s\max} = \frac{R_b + R_p}{2(U_b^* + v_t)} \ln\left[\frac{1 - \cos(\frac{\pi}{2} + \theta_p)}{1 + \cos(\frac{\pi}{2} + \theta_p)} \times \frac{1 + \cos\theta_p}{1 - \cos\theta_p}\right] \tag{9.28}$$

In industrial flotation machines it is not uncommon to find bubbles loaded so that a considerable fraction of their available surface area is covered by adhering particles. If this were not so, the recovery rate of floated material would be uneconomically low. The sweeping action on the adhering particles and the steady loading of the bubble surface from below is graphically illustrated in the sequence of photographs of a single bubble during its lifetime in a flotation pulp that is shown in Figure 9.2. When the layer of attached particles builds up past the equator of the bubble, the available sliding time is shortened as shown in Figure 9.7. When the bubble is more than 50% loaded, equation 9.28 becomes

$$t_s = \frac{R_b + R_p}{2(U_b^* + v_t)} \ln\left[\frac{1 - \cos\theta_L}{1 + \cos\theta_L} \times \frac{1 + \cos(\theta_c + \theta_p)}{1 - \cos(\theta_c + \theta_p)}\right] \tag{9.29}$$

L is the fractional loading on the bubble.

$$L = \frac{\text{Fraction of bubble surface covered by adhering particles}}{\text{Total bubble surface area}}$$
$$L = \frac{1}{2}(1 + \cos\theta_L) \tag{9.30}$$

θ_L is called the loading angle.

The corresponding value for t_{smax} is

$$t_{s\max} = \frac{R_b + R_p}{2(U_b^* + v_T)} \ln\left[\frac{1 - L}{L} \times \frac{1 + \cos(\theta_L + \theta_p)}{1 - \cos(\theta_L + \theta_p)}\right] \tag{9.31}$$

While it is possible to calculate the sliding time at least approximately for particles of arbitrary size and density when the bubble size is known, the same cannot be said for the induction time. The sliding time is governed primarily by physical factors and the hydrodynamics in the water phase close to the bubble. The induction time, on the other hand, is influenced strongly by the chemical conditioning of particle surface. In particular the contact angles, advancing and receding, play an important role. In addition the precise shape of the particle as well as the roughness of its surface and the mineralogical composition and texture of its surface all contribute strongly to the time that it takes for stable attachment to occur.

Three stages in the attachment process have been identified: thinning of the water film between the particle and the bubble, actual rupture of the bubble skin when the thinning film reaches an unstable condition and finally the retraction of the water from the particle surface to form a stable three-phase contact perimeter. Of these sub-processes only the first and third contribute to the induction time.

The rupture of the film is much quicker and the rupture time is usually neglected by comparison to the time taken for film drainage and the formation of the stable three-phase contact perimeter.

In spite of considerable research effort, there are no quantitative models available that allow the calculation of the induction time for a specific particle. However, it can be assumed that the induction time is dominated by the particle characteristics such as advancing and receding contact angles, mineralogical texture of the surface particle shape and surface roughness. The induction time is not significantly influenced by the hydrodynamic conditions of the collision nor by the bubble size. This is not completely true because the exact orientation of the particle relative to the bubble surface on first contact is known to influence the film drainage process. In spite of this it is postulated that the induction time is entirely a particle-specific constant. Each particle in the flotation cell has its own unique value of induction time which remains the same for every collision that the particle makes with a bubble during its lifetime in the flotation environment. At least any variation in the induction time that a particular particle experiences from collision to collision will reflect only small statistical fluctuations around an average value.

This postulate of particle specificity for the induction time leads to an important conclusion relating to the kinetics of the overall flotation process. If any particle has an induction time larger than the sliding time associated with a direct center line collision with the largest available bubble, it will never float no matter how long it remains in the flotation cell. This gives rise to the concept of a non-floatable component for every type of particle. This behavior is commonly observed during kinetic studies on flotation systems and has been routinely applied to the analysis of flotation kinetics since at least the 1950s and probably much earlier than that.

Non floatable particles will be found in virtually any flotation environment from precisely controlled Hallimond tubes through to large industrial flotation cells. The only exception will be in situations where the particles are conditioned to have very hydrophobic surfaces so that they all have induction times short by comparison with available sliding times. Under these conditions particle capture is dominated by the collision process and this is often exploited to measure the collision efficiency experimentally.

The collision and sliding phenomena that are described above are illustrated graphically in the sequence of photographs in Figure 9.2 which show a single bubble during its sojourn in a fairly typical flotation environment. These photographs show clearly that the particles slide over the front surface of the bubble and accumulate in the lower hemisphere. The close packing of the particles reflects their ability to form stable particle-particle agglomerates because of their hydrophobic character. The layer of packed particles gradually builds up on the bubble and eventually encroaches on the upper hemisphere where it reduces the sliding time as the load on the bubble increases. Once the particle layer crosses the equator of the bubble, the bubble loading starts to impact the rate of transfer of particles to the bubble phase and this must be taken into account when developing models based on the flotation kinetics.

8.3 **Distributed Rate Constant Kinetic Model for Flotation**

The kinetic model for flotation is based on equation 9.3. This equation shows clearly that the rate of transfer of particles of type *ij* from the pulp phase to the bubble phase is first order with respect to the concentration of these particles in th pulp phase. This observation leads to a simple formulation of the kinetic law as

$$\text{Rate of transfer of particles of type } ij = K_{ij}C_{ij} \tag{9.32}$$

where

$$\begin{aligned} K_{ij} &= \frac{3}{2}(D_p + d_{pi})^2(U_b + v_{Tij}) \times \frac{G_v \tau_b}{D_b^3} \times E_{Cij}E_{Aij}(1 - E_{Dij}) \\ &= \frac{1}{4}\left(1 + \frac{d_{pi}}{D_b}\right)^2 (U_b + v_{Tij}) \times S_v \times E_{Cij}E_{Aij}(1 - E_{Dij}) \\ &= \kappa_{ij} S_v \end{aligned} \tag{9.33}$$

and

$$S_v = \frac{6G_v\tau_b}{D_b} \qquad \text{m}^2 \text{ bubble surface/m}^3 \text{ cell} \tag{9.34}$$

is the total bubble surface area in contact with the pulp phase per unit volume of the cell. It is easy to see from equation 9.33 that K_{ij} has units of s^{-1}. K_{ij} is a complex function of particle size and particles density because of the complex dependence of E_{Cij} and E_{Aij} on the size of the particles. κ_{ij} is a mass transfer coefficient for transfer of particles from the pulp to the surface of the bubbles and it can be scaled independently of the bubble surface area. κ_{ij} has units of m/s.

Equation 9.33 appears to be a perfectly conventional linear kinetic law but the Sutherland principle imparts a special character to K_{ij}. A definite fraction of the particles of type *ij* (i.e. particles characterized by size d_{pi} and mineralogical grade g_j) have $K_{ij} = 0$ because $t_{ind} > t_{s\max}$ for these particles and therefore $E_{Aij} = 0$. This is the non-floatable fraction for this particle type.

The size of the non floatable fraction depends on the distribution of induction times across the population of particles that are characterized by size d_{pi} and mineralogical composition *g*. There is apparently no experimental data from which these distributions can be estimated although experimental techniques have been developed for the measurement of induction times. Since the induction time cannot be negative, it is reasonable to postulate that its value has a gamma distribution defined by the probability density function

$$f_{ij}(t_{ind}) = \frac{t_{ind}^{\beta_{ij}-1} \exp\left(-\frac{t_{ind}}{\tau_{ij}}\right)}{\tau_{ij}^{\beta_{ij}} \Gamma(\alpha_{ij})} \tag{9.35}$$

which has two parameters β_{ij} and τ_{ij} that vary with size particle size and particle composition.

The fraction of the particles in class *ij* that are non floatable is usually specified in terms of the ultimate recovery, $\Re_{ij}$, of particles of this type

$$\Re_{ij} = \text{Prob}\{t_{ind} < t_{s\max}\} \tag{9.36}$$

where $t_{s\,max}$ is the longest sliding time available and is given by equation 9.28.
Using equations 9.35 and 9.36, the ultimate recovery of particles of type *ij* is given by

$$\Re_{ij} = \frac{\Gamma_z(\beta_{ij})}{\Gamma(\beta_{ij})} \tag{9.37}$$

Where Γ_z is the incomplete gamma function and

$$z = \frac{t_{s\max}}{\tau_{ij}} \tag{9.38}$$

The parameters α_{ij} and τ_{ij} in the distribution of induction times are related uniquely to the mean and variance of the distribution.

$$\tau_{ij} = \frac{\text{Variance}}{\text{Mean}} = \frac{\sigma_{ind}^2}{\bar{t}_{ind}} \tag{9.39}$$

$$\beta_{ij} = \frac{\text{Mean}}{\tau_{ij}} = \frac{\bar{t}_{ind}^2}{\sigma^2} \tag{9.40}$$

$\bar{t}_{ind}$ is the average of the induction time distribution and σ_{ind}^2 its variance.
The specific flotation constant for the floatable component of particles of type *ij* is given by equation 9.33 with the appropriate value of the attachment efficiency E_{Aij}.

The attachment efficiency for the floatable fraction of particles of type *ij* is given by

$$E_{Aij} = \text{Prob}\{t_s - t_{ind} > 0\} \tag{9.41}$$

Equation 9.41 contains two random variables t_{ind} and t_s and the indicated probability can be evaluated from their respective density functions.

The sliding time t_s inherits its randomness from the collision angle θ_c which is turn inherits its

randomness from the position of the particles relative to the axis of the bubble motion. θ_c has probability distribution function given by equation 9.22 and distribution density function

$$f_{\theta_c}(\theta_c) = \cos\theta_c \tag{9.42}$$

t_s is related to θ_c by equation 9.27 and its distribution density function is

$$f_{t_s} = \frac{f_{\theta_c}(\theta_c)}{\left|\frac{dt_s}{d\theta_c}\right|} \tag{9.43}$$

Thus

$$\begin{aligned} E_{Aij} &= \int_0^{t_{s\max}} \int_0^{t_s} f_{t_s}(t_s) \times f_{ij}(t_{ind})\, dt_{ind}\, dt_s \\ &= \int_0^{t_s\max} f_{\theta_c}(\theta_c) \times F_{ij}(t_s)\, d\theta_c \\ &= \int_0^{\frac{\pi}{2}} \cos\theta_c \times F_{ij}(t_s)\, d\theta_c \end{aligned} \tag{9.44}$$

where f_{ij} is the distribution density function for the induction time given by equation 9.35 and F_{ij} is the corresponding distribution function. In practical applications the integral in equation 9.44 must be evaluated numerically but this is comparatively easy to do.

8.4 **Bubble loading during flotation**

Up to now the discussion of the kinetic model for flotation has been presented from the point of view of the particles. Some additional considerations emerge when the process is viewed from the point of view of the bubble. As the bubble rises through the pulp phase, it adds to its load of particles and the lower hemisphere of the bubble becomes increasingly covered with accumulated attached particles as a result of successful collisions. The sequence of photographs in Figure 9.2 show this accumulation process in graphic detail.

This loading process can be quantitatively modeled using the kinetic model of particle capture that was described in the previous section. As a bubble rises through the well-mixed pulp it collides with all types of particles some of which are captured according to the model that has been developed. The different types of particle will be captured at different rates depending on their size and hydrophobicity which determine their specific flotation rate constant. The bubble accordingly accumulates a load that has a particle composition and size distribution that is distinctly different to the average particle composition of the pulp. However, during the lifetime of a particular bubble the pulp environment does not change so that the bubble becomes increasingly covered with a load of particles of size and composition distribution that does not change with bubble residence time.

The surface area of the bubble that is occupied by an adhering particle depends primarily on the shape of the particle but also depends on the packing density of the particles on the curved bubble surface. Hydrophobic particles form agglomerates in suspension even when no bubble surface is present and this phenomenon can increase the bubble surface loading. Evidence of these agglomerates can be seen in the photograph of a heavily loaded bubble in Figure 9.8. The lower hemisphere of the bubble is covered by several layers of particles where evidently not every particle is in contact with the bubble surface.

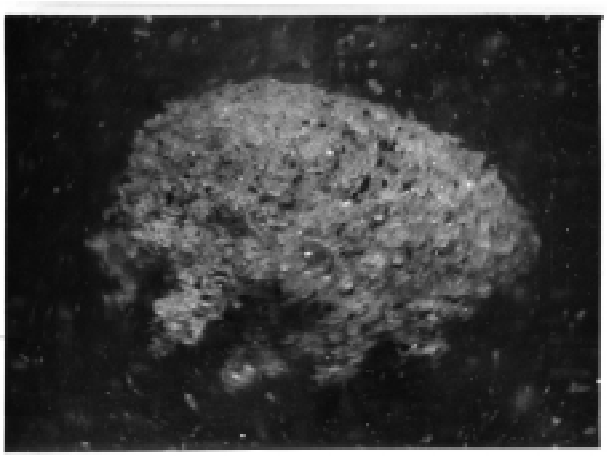

Figure 9.8 *Fully loaded bubble showing particle agglomerates. Photo from King et al. (1974)*

A model for bubble loading by particles on its surface can be based on the specific coverage achieved by each type of particle.

Let η_{ij} be the load per unit volume of bubble on a bubble fully loaded with particles of type *ij*

$$\eta_{ij} = \frac{(1 - \varepsilon_{ij})3(R_b + R_{pi})^2 R_{pi}\rho_{ij} + \eta_0}{R_b^3} \quad \text{kg/m}^3 \text{ bubble volume} \tag{9.45}$$

ε_{ij} is the packing voidage for particles of type *ij* and ρ_{ij} is the density of particles of type *ij* and η_0 is the load on a very small bubble that is composed largely of agglomerates of hydrophobic particles.

A fully loaded bubble in a flotation pulp carries a load given by

$$L_{\max} = V_b \sum_{ij} m_{ij}\eta_{ij} \tag{9.46}$$

where V_b is the volume of a bubble and m_{ij} is the mass fraction of particles of type *ij* in the bubble load.

$$L_{\max} = 4\pi \sum_{ij} (1 - \varepsilon_{ij}) m_{ij} R_{pi}\rho_{ij}(R_b + R_{pi})^2 + \eta_0 \tag{9.47}$$

L_{max} can be measured by capturing single completely loaded bubbles and weighing the bubble load. For very small bubbles the maximum load is approximately independent of the bubble volume and for bubbles that are much larger than the particle size, L_{max} varies approximately as $V_b^{2/3}$. If the particles are all of the same size and density.

$$L_{\max} = a(R_b + R_{pi})^2 + \eta_0 \tag{9.48}$$

Some data from captured fully loaded bubbles are given in Figure 9.9.

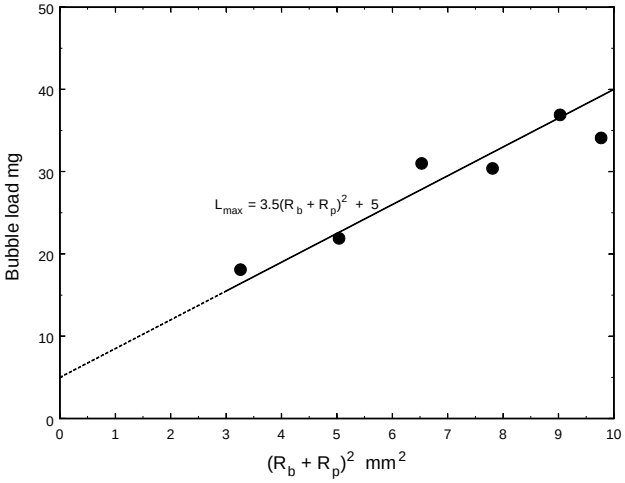

Figure 9.9 *Measured load on fully loaded single bubbles. Data from King et al. (1974)*

The development of the bubble load L is described by the following differential equation as the bubble moves through the pulp phase and its residence time increases.

$$\frac{6G_v\tau_b L_{\max}}{D_b}\frac{dL}{d\tau} = \sum_{ij} K_{ij} C_{ij} \qquad (9.49)$$

with K_{ij} given by equation 9.33 and tau representing the bubble residence time..

During the first few seconds of the loading process $L < 0.5$ and the right hand side of equation 9.49 is constant and the bubble load increases linearly with bubble residence time As the load on the bubble increases, the rate of loading decreases as a result of two effects. As the solid load carried by the bubble increases, its rise velocity decreases because of its increased mass. Since K_{ij} is proportional to U_b according to equation 9.33, it decreases as the rise velocity decreases. When the load on the bubble exceeds 50%, K_{ij} decreases with increase in bubble load because the sliding time, and therefore E_{Aij}, decreases according to equation 9.28. The sliding time eventually becomes zero as the bubble approaches complete loading.

Under these conditions of inhibited flotation the bubble transports a load of particles to the froth phase that is limited either by the surface capacity of the bubbles or by the lifting power of the bubble. It should however always be considered in industrial flotation applications because economic considerations usually dictate that industrial flotation cells be operated at significant bubble loadings.

8.5 Rise times of loaded bubbles.

In order to quantify the effect of bubble loading on the specific rate of flotation it is necessary to calculate the bubble rise velocity as a function of the load that is carried by the bubble. Light particles rise in water at terminal velocities that are lower than that calculated from the drag coefficient for heavy particles that sink. Deformable bubbles have terminal rise velocities that are still lower. Very small bubbles rise in water as though they behaved as rigid spheres having the density of air. Larger bubbles deform while they rise and become ellipsoidal in shape. This is evident in the photographs in Figure 9.2. Still larger bubbles have a spherical cap shape. The drag coefficient varies accordingly.

In spite of these anomalies, the terminal rise velocities of bubbles can be accurately calculated using the drag coefficient for lighter-than-water solid spheres provided that the bubble Reynolds number is calculated using the horizontal projection of the bubble diameter. The diameter of the horizontal projection of the bubble can be calculated from the effective volume diameter using the empirical

relationship

$$\frac{D_{be}}{D_{bh}} = \frac{1 + 0.60Ta^3}{1 + Ta^3} \tag{9.50}$$

where

$$Ta = Re_{be}Mo^{0.23} \tag{9.51}$$

$$Re_{be} = \frac{D_{be}U_b\rho}{\mu} \tag{9.52}$$

$$D_{be} = \left(\frac{6V_b}{\pi}\right)^{\frac{1}{3}} \tag{9.53}$$

and V_b is the bubble volume. *Mo* is the Morton number and is defined as

$$Mo = \frac{g\mu^4}{\rho\sigma^3} \tag{9.54}$$

where σ is the surface tension of the solution at the bubble surface.

The terminal rise velocity of a partly loaded bubble can be calculated from

$$\begin{aligned} U_b &= \left(\frac{8(V_b\rho_w - m_b)g}{C_D\pi D_{bh}^2\rho_w}\right)^{\frac{1}{2}} \\ &= \frac{D_{be}}{D_{bh}}\left(\frac{4(\rho_w - LL_{\max})gD_{be}}{3C_D\rho_w}\right)^{\frac{1}{2}} \end{aligned} \tag{9.55}$$

where C_D is the drag coefficient for a rising bubble.

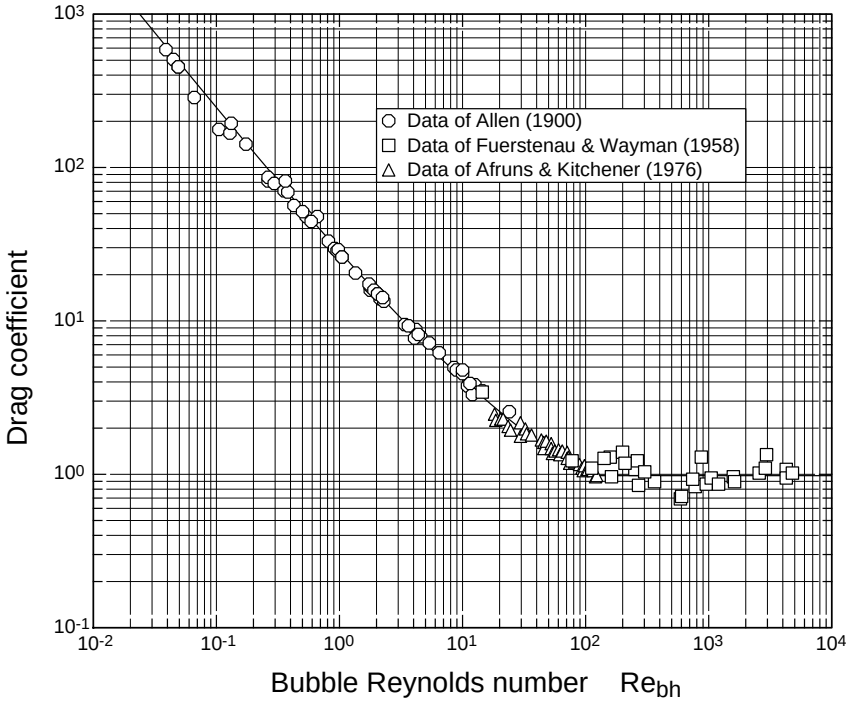

Figure 9.10 *Drag coefficient for rising bubbles in viscous fluids. Experimental data from Allen (1900), Fuerstenau and Wayman (1958) and Afruns and Kitchener(1976). Solid line represents data for rising solid spheres.*

Experimental data measured on rising bubbles in water containing surfactant reveals that C_d shows the same variation with bubble Reynolds number as solid lighter-than-water spheres provided that due allowance is made for the deformation of the bubble. The data is shown in Figures 9.10 and 9.11 where the measured drag coefficient is plotted against the bubble Reynolds number calculated using the horizontally projected bubble velocity

$$Re_{bh} = \frac{D_{bh} U_b \rho_w}{\mu_w} \tag{9.56}$$

The line in Figures 9.10 and 9.11 represents the drag coefficient for rising solid spheres and is given by

$$\begin{aligned} C_D &= 0.28\left(1 + \frac{9.06}{Re_{bh}^{½}}\right)^2 \qquad \text{for } Re_{bh} \le 108 \\ &= 0.98 \qquad\qquad\qquad\qquad\quad \text{for } Re_{bh} > 108 \end{aligned} \tag{9.57}$$

The corresponding equation for the line in Figure 9.11 is

$$C_D = 0.28\left(\frac{(1+0.0921\Phi^{½})^{½}+1}{(1+0.0921\Phi^{½})^{½}-1}\right)^2 \quad \text{for } \Phi < 1.14\times10^4 \tag{9.58}$$

Figure 9.11 is useful because it can be used to calculate the terminal rise velocity of the bubble without trial and error methods because at terminal settling velocity.

$$C_D Re_{bh}^2 = \frac{4}{3}\frac{(\rho_w - LL_{\max})\rho_w g D_{be}^3}{\mu^2} \tag{9.59}$$

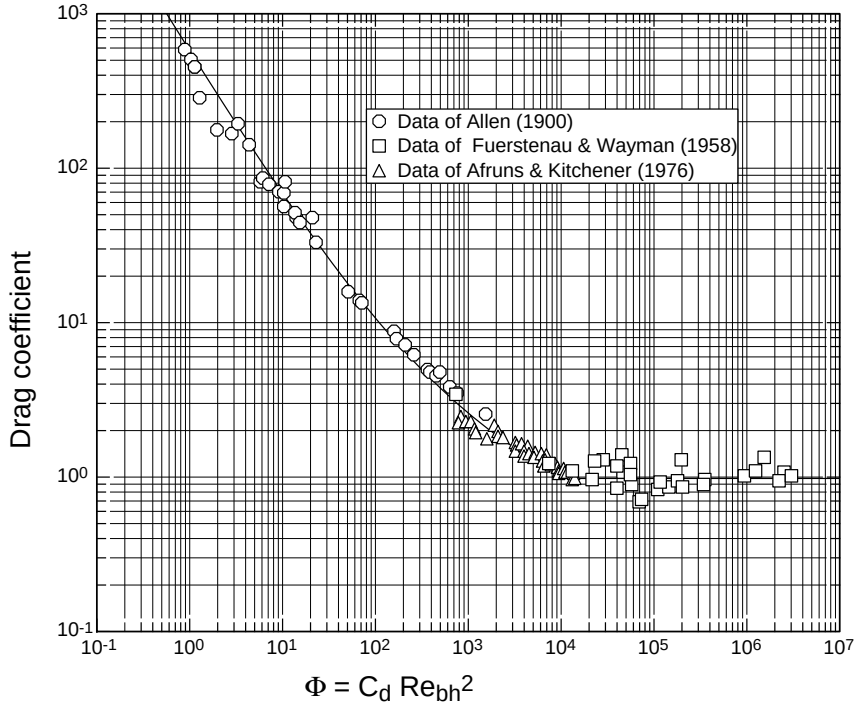

Figure 9.11 *Drag coefficient for rising bubbles in viscous fluids. Experimental data from Allen (1900), Fuerstenau and Wayman (1958) and Afruns and Kitchener (1976). Solid line represents data for rising solid spheres. This coordinate system is most useful for the calculation of the terminal rise velocity of bubbles.*

This can be calculated without knowing the rise velocity and the value of C_D can be obtained direct from Figure 9.11. This provides a method to calculate the terminal rise velocity of the bubble as its load of solid increases.

The application of these methods is described using the following illustrative examples.

Illustrative example 9.1

Calculate the terminal rise velocity of the following bubbles in a dilute aqueous solution of butanol

having surface tension 0.052 N/m. The density of the water is 999.1 kg/m^3, and its viscosity 0.001 kg/ms.

a) Small bubble of volume effective diameter = 0.5 mm

$$\Phi = C_D Re_{bh}^2 = \frac{4}{3}\frac{\rho_w^2 g D_{be}^3}{\mu^2}$$

$$= \frac{4}{3}\frac{999.1^2 \times 9.81 \times (0.5 \times 10^{-3})^3}{(0.001)^2}$$

$$= 1.63 \times 10^3$$

The value of C_D can now be evaluated from Figure 9.11 or the equation

$$C_D = 0.28\left(\frac{(1 + 0.0921 \times (1.63 \times 10^3)^{1/2})^{1/2} + 1}{(1 + 0.0921 \times (1.63 \times 10^3)^{1/2})^{1/2} - 1}\right)^2$$

$$= 2.05$$

Bubbles of this small size will maintain a spherical shape while rising in water, thus we try D_{be}/D_{bh} as a first estimate.

From equation 9.55

$$U_b = \left(\frac{4 \times 9.81 \times 0.5 \times 10^{-3}}{3 \times 2.05}\right)^{1/2} = 0.056$$

Check the value of D_{be}/D_{bh}:

$$Mo = \frac{9.81 \times (0.001)^4}{999.1 \times (0.052)^3} = 6.98 \times 10^{-11}$$

$$Re_{be} = \frac{0.5 \times 10^{-3} \times 0.056 \times 999.1}{0.001}$$

$$= 28.0$$

$$Ta = 28.0 \times (6.98 \times 10^{-11})^{0.23}$$

$$= 0.129$$

From equation 9.50

$$\frac{D_{be}}{D_{bh}} = \frac{1 + 0.6 \times 0.129^3}{1 + 0.129^3} = 0.999$$

which confirms the estimate.

The calculated value can be compared to the value of 0.042 m/s measured by Allen for a 0.48-mm diameter bubble in water.

b) Intermediate bubble of effective volume diameter = 2 mm

$$\Phi = C_D Re_{bh}^2 = \frac{4}{3}\frac{999.1^2 \times 9.81 \times (2 \times 10^{-3})^3}{(0.001)^2}$$
$$= 1.044 \times 10^5$$

Since $\Phi > 1.14 \times 10^4$, $C_D = 0.98$

A bubble of 2-mm diameter in water is elliptical in shape, and the value of the ratio D_{be}/D_{bh} must be calculated. This requires some iterative calculation. Start the calculation at an intermediate value of $D_{be}/D_{bh} = 0.8$.

$$U_{10} = \frac{D_{be}}{D_{bh}}\left(\frac{4 \times 9.81 \times 2 \times 10^{-3}}{3 \times 0.98}\right)^{1/2}$$
$$= 0.8 \times 0.163 \text{ m/s}$$

The diameter ratio must now be refined.

$$Re_{be} = \frac{2 \times 10^{-3} \times 0.8 \times 0.163 \times 999.1}{0.001}$$
$$= 261$$
$$Ta = 261 \times (6.98 \times 10^{-11})^{0.23}$$
$$= 1.204$$
$$\frac{D_{be}}{D_{bh}} = \frac{1 + 0.6 \times 1.204^3}{1 + 1.204^3} = 0.746$$

Refining the value of U_b using this value for the diameter ratio gives

$$\frac{D_{be}}{D_{bh}} = 0.76$$

and

$$U_b = 0.76 \times 0.163 = 0.124 \text{ m/s}$$

This answer can be compared to the value of 0.136 m/s measured by Fuerstenau and Wayman (1958) for a 1.97-mm bubble in water.

c) Large bubble having volume effective diameter = 12 mm

Bubbles as large as this will have a spherical cap shape, and therefore $C_D = 0.98$ and the diameter ratio has the limiting value 0.6

$$U_b = 0.6\left(\frac{4 \times 9.81 \times 12 \times 10^{-3}}{3 \times 0.98}\right)^{1/2}$$
$$= 0.24 \text{ m/s}$$

This can be compared with the value 0.236 m/s measured by Fuerstenau and Wayman for a bubble having a volume effective diameter of 12.2 mm.

Illustrative example 9.2

Calculate the terminal rise velocity of a 0.5-mm diameter air bubble that is carrying 5 galena particles that may be taken as cubes of side 100 μm. The density of galena is 7500 kg/m^3. The specific load carried by the bubble is

$$\frac{5 \times (100 \times 10^{-6})^3 \times 7500}{\frac{\pi}{6}(0.5 \times 10^{-3})^3} = 573.0 \text{ kg/m}^3$$

$$\Phi = C_D Re_{bh}^2 = \frac{4}{3} \frac{(999.1 - 573.0)\, 999.1 \times 9.81 \times (0.5 \times 10^{-3})^3}{(0.001)^2}$$

$$= 696$$

$$C_D = 0.28 \left(\frac{(1 + 0.0921 \times 696^{1/2})^{1/2} + 1}{(1 + 0.0921 \times 696^{1/2})^{1/2} - 1} \right)^2$$

$$= 11.21$$

$$U_b = \left(\frac{4(999.1 - 573.0)\ 9.81 \times 0.5 \times 10^{-3}}{3 \times 11.21 \times 999.1} \right)^{1/2}$$

$$= 0.016 \text{ m/s}$$

which is about 1/3 of the rise velocity of an unloaded bubble.

Illustrative Example 9.3

Calculate the specific flotation rate constant for 100 μm galena particles on 0.5 mm diameter bubbles in a continuous flotation cell that is aerated at 0.013 m^3 air/m^3 pump. The bubble residence time is 5s. Consider the case where the average induction time for the particles is 100 ms. Calculate the fraction of the non floatable component for these particles. Consider the case when the bubble is carrying 5 galena particles.

Solution

Calculate the terminal settling velocity of the pyrite particles which may be assumed to be cubic in shape. See illustrative example 3.4

$$d_e = \left(\frac{6\nu_p}{\pi} \right)^{1/3} = \left(\frac{6 \times 10^{-12}}{\pi} \right)^{1/3} = 1.241 \times 10^{-4} \text{ m}$$

$$\nu = \frac{\pi d_e^2}{a_p} = \frac{\pi(1.241 \times 10^{-4})^2}{6 \times 10^{-8}} = 0.806$$

$u_T = 0.022$ m/s

From illustrative example 9.2, the bubble rise velocity = 0.030 m/s.

Calculate E_c:

$$r_p' = \frac{R_p}{R_b} = \frac{0.05}{0.25} = 0.2$$

$$Re_b = \frac{D_b U_b \rho_w}{\mu_w} = \frac{0.5 \times 10^{-3} \times 0.030 \times 999.1}{0.001} = 14.9$$

From equation 9.8

$$\alpha = \exp\left(- \frac{4 \times 14.9^{0.72}}{45} \cdot \frac{0.2}{1.2} \right)$$

$$= 0.901$$

$$U_b^* = 0.030 \left[\frac{3}{2}(1 - 0.901 + 0.901 \times 0.2) + \left(\frac{1}{2} - \frac{3}{4} \times 0.901 \right)_{0.2}^{2} \right]$$

$$= 0.0124$$

$$E_c = 3(1 - \alpha) r_p' + \frac{3}{2} \alpha r_p'^2$$

$$= 3(1 - 0.901)\, 0.2 + \frac{3}{2} 0.901 \times 0.2^2$$

$$= 0.114$$

$$m_p = 5 \times (100 \times 10^{-6})^3 \times 7500$$

$$= 3.75 \times 10^{-8}$$

$$= 0.0375 \times 10^{-6}$$

$$V_b = \frac{\pi}{6} (0.5 \times 10^{-3})^3$$

$$= 6.545 \times 10^{-11}$$

Assuming the cubic particles pack closely together on the bubble, they occupy a total area = 5×10^{-8} m^2. The total surface area of the bubble is $\pi(0.5 \times 10^{-3})^2 = 7.85 \times 10^{-7}$ m^2.

$$\text{Fractional load on bubble} = L = \frac{5 \times 10^{-8}}{7.85 \times 10^{-7}} = 0.064$$

Since this less than half load, t_{smax} is calculated from equation 10.24

$$\theta_p = \frac{R_p}{R_b + R_p}$$

$$= \frac{5.0 \times 10^{-6}}{0.25 \times 10^{3} + 5.0 \times 10^{-6}}$$

$$= 0.167 \text{ radians}$$

$$t_{smax} = \frac{0.25 \times 10^{-3} + 50 \times 10^{-6}}{2(0.0124 + 0.022)} \ln \left[\frac{1 - \cos\left(\frac{\pi}{2} + 0.167\right)}{1 + \cos\left(\frac{\pi}{2} + 0.167\right)} \times \frac{1 + \cos(0.167)}{1 - \cos(0.167)} \right]$$

$$= 4.35 \times 10^{-3} \times \ln [1.40 \times 142.8]$$

$$= 0.023 \text{ s}$$

E_A is evaluated by numerical integration of equation 9.44.

$$E_A = \int_0^{\frac{\pi}{2}} \cos\theta_c \times F_{ind}(t_s)\, d\theta_c = 0.636$$

The specific rate constant for transfer from pulp to bubble phase can be calculated from equation 9.33.

$$k = \frac{3}{2}(1 + r')^2 (U_b + \nu_T) \times E_C \times E_A$$

$$= \frac{3}{2}(1 + 0.2)^2 (0.030 + 0.022) \times 0.114 \times 0.636$$

$$= 8.14 \times 10^{-3} \text{ m/s}$$

$$K = \frac{G\tau_b}{D_b} k$$

$$= \frac{0.013 \times 5}{0.5 \times 10^{-3}} \times 8.14 \times 10^{-3}$$

$$= 1.06 \text{ s}^{-1}$$

These calculated rate constants apply only to those particles in the pulp that have an induction time smaller than t_{smax}. The remainder make up the non floatable component. The fraction of pyrite particle that are non floatable is calculated from the equation 9.37.

$$\beta = \frac{\text{Average induction time}^2}{\text{Variance of induction time}}$$

$$= \frac{(100 \times 10^{-3})^2}{90 \times 10^{-3}}$$

$$= 0.111$$

$$\bar{t}_s = \frac{90 \times 10^{-3}}{100 \times 10^{-3}} = 0.9 \text{ s}$$

$$z = \frac{t_{smax}}{\bar{t}_s} = \frac{0.023}{0.9} = 0.0255$$

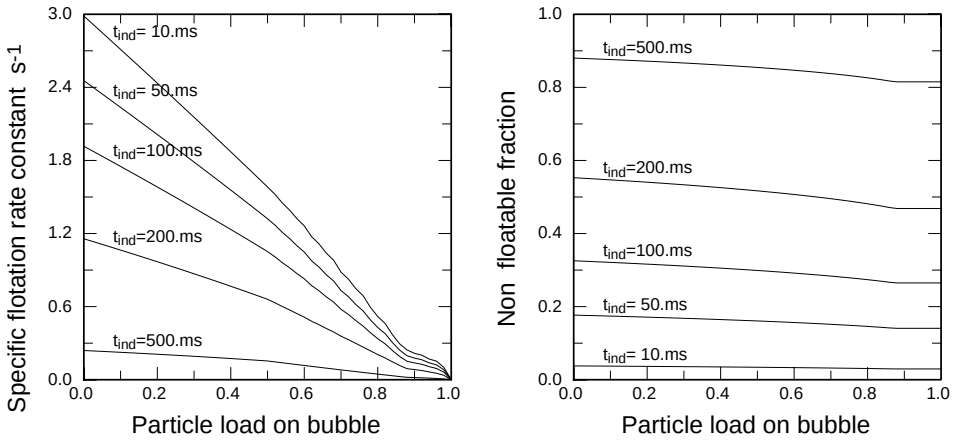

Figure 9.12 *Calculated values of the specific flotation rate constant and the corresponding non floatable fraction for 100 µm galena particles on 0.5 mm diameter bubbles. The parameter is the average of the induction time distribution for the particles.*

These calculations can be repeated throughout the range of possible values of the parameter $\bar{t}_{ind}$ and for different particle loads on the bubble. The results are shown in Figure 9.12. The decrease in flotation rate constant with increase in the particle load is clearly evident in Figure 9.12. While the load is less the 50%, both the collision and attachment efficiencies remains constant because the colliding particle does not receive any interference from the adhering particles which are all on the lower hemisphere of the bubble. The decrease in the rate constant is due entirely to the reduction in the bubble rise velocity as the load of particles increases. Once the load exceeds 50%, the attachment efficiency decreases as the available free bubble surface on the upper hemisphere reduces and the rate constant decreases more rapidly. The rate constant reduces to close to zero when the load reaches a mass that the bubble is unable to lift and the number of collisions is reduced to a small number that is governed by the settling velocity of the solid particles in the pulp.

Since there are bubbles in all states of loading in the flotation cell, an average bubble loading must be calculated to fix the value of K_{ij} for the pulp volume as a whole. A method for doing this is described in connection with the simplified model in Section 9.8

8.6 **Particle Detachment**

In the previous sections it has been assumed that if a particle collides with and adheres to a bubble it will enter the froth phase when the carrying bubble breaks through the pulp froth interface. This is not necessarily so because a particle can become detached from a bubble due to the effects of stresses that are induced by the turbulence in the flotation cell. The detachment process is complex and no comprehensive analysis is available. Two forces are dominant in causing a particle to become detached from a bubble. The weight of the particle and the inertia of the particle during the acceleration of the bubble that is induced by turbulent eddies in the fluid. The distortion of the

bubble due to the weight of the particle is illustrated in Figure 9.13. The bubble is distorted and the three phase contact line is pulled back over the particle until a position of equilibrium is established or until the bond between particle and bubble is broken. In the ideal situation that is illustrated in Figure 9.13,the separating force F_g is balanced by the vertical component F_c of the surface tension force F_σ. If the separating force exceeds the maximum value that F_c can achieve, the particle will be detached. The maximum value of F_c is obtained as follows.

$$F_c = \sigma 2\pi R_p \sin\beta \sin\varphi \tag{9.60}$$

This must be maximized subject to the condition that $\beta + \varphi = \theta$ where θ is the contact angle. Setting the derivative of F_c equal to zero shows that F_c is maximized when

$$\varphi = \beta = \frac{\theta}{2} \tag{9.61}$$

$$F_{c\max} = 2\pi R_p \sigma \sin^2\left(\frac{\theta}{2}\right) \tag{9.62}$$

The largest particle that can attach to the bubble in a quiescent pulp is given by

$$\frac{\pi}{6} d_{p\max}^3 g(\rho_s - \rho_w) = \pi d_{p\max} \sigma \sin^2\left(\frac{\theta}{2}\right) \tag{9.63}$$

$$d_{p\max} = \left(\frac{6\sigma}{g(\rho_s - \rho_w)}\right)^{\frac{1}{2}} \sin\left(\frac{\theta}{2}\right) \tag{9.64}$$

The additional forces caused by turbulence can detach a smaller particle and an approximate analysis by Woodburn *et al.* (1971) leads to the following model for the detachment efficiency.

$$E_D = \left(\frac{d_p}{d_{p\max}}\right)^{1.5} \tag{9.65}$$

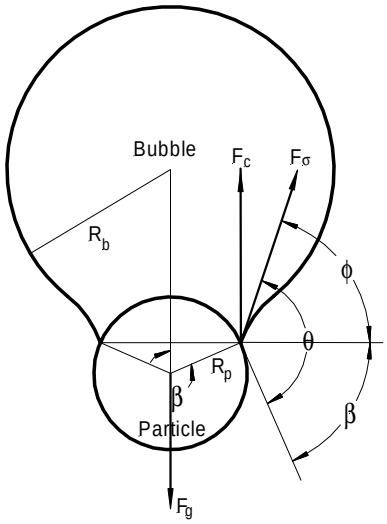

Figure 9.13 *Distortion of a bubble due to weight of an attached particle. Adapted from Drzymala (1994)*

8.7 The Froth Phase

8.7.1 Motion of the froth

The kinetic models for the collection of solid particles in the pulp are not adequate to describe the overall behavior of the flotation cell because the froth on the top of the cell exerts a strong influence on the kinetic behavior of the flotation system. The processes that take place in the froth phase are complex and they ultimately determine whether a particle that is captured by a bubble in the pulp phase will be recovered in the concentrate stream from the flotation cell. Two aspects of froth behavior must be considered: the motion of the froth from the surface of the pulp towards the upper

surface of the froth and the concentrate overflow weir and the processes that occur within the froth while it is flowing. These processes include bubble bursting, particle detachment and drainage of water and solids from the froth. It is useful to consider the motion of the froth first and then superimpose the internal subprocesses on the basic flow pattern.

Bubbles, carrying their loads of attached particles, leave the pulp phase and pass into the froth phase at the pulp-froth boundary at the top of the pulp. The bubbles do not burst immediately and they congregate together and float on the surface of the pulp. The bubbles are pushed upward steadily by the arrival of new bubbles from the pulp phase. Provided that the bubbles are not too large, they retain their spherical shape as they pass from the pulp into the lower layer of the froth phase. They tend to arrange themselves in a hexagonal close-packed arrangement with the intervening spaces between the bubbles filled with liquid that is carried upward with the bubble from the pulp phase. This interstitial liquid entrains significant quantities of particulate material from the pulp and the entrained material can include significant quantities of hydrophilic non floating particles. The composition of the entrained solids is determined primarily by the composition of the solid that is suspended in topmost regions of the pulp phase.

The interstitial water drains quite rapidly from the froth and the bubbles move closer together and deform steadily to take up polyhedral shapes as the films that separate any two bubbles become thinner and more or less flat. The few layers of spherical bubbles immediately above the pulp surface can usually be neglected when considering the froth phase as a whole unless the froth layer is very thin. As the interstitial water drains the structure becomes a true froth with a characteristic geometrical structure that is illustrated in two dimensions in Figure 9.14. Three lamellar films that separate the bubbles meet to form edges called Plateau borders that form a network of channels through which water can drain from the froth under gravity. The radius of curvature of the lamellar films is considerably larger than the radii of the walls of the Plateau borders as illustrated in Figure 9.14. This means that the pressure inside a Plateau border is less than the pressure inside the laminar films to which it is attached. Consequently water drains from the lamellar films into Plateau borders and the films become steadily thinner. The plateau borders vary in length, cross-sectional area and orientation throughout the froth. The films that separate the bubbles contain all particles that were attached to a bubble when the bubble passed from the pulp phase into the froth.

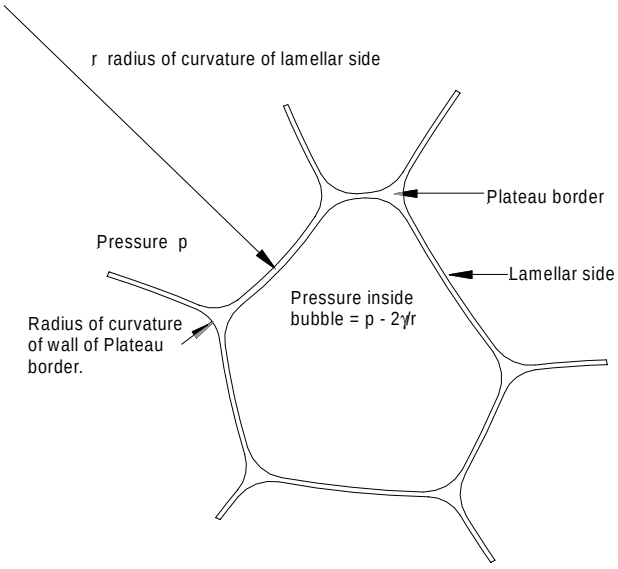

Figure 9.14 *Geometrical structure of a single bubble in a froth shown here in 2 dimensions.*

The bubbles continue to move upward toward the top surface of the froth and laterally toward the concentrate overflow weir from which the particle-laden froth is recovered into the concentrate. Some of the bubbles reach the top surface of the froth where they burst and so never reach the concentrate overflow. The motion of the froth phase can be modeled as a two-dimensional potential flow problem. This is illustrated in Figure 9.15 and 9.16 which show a vertical cross-section through the froth phase on top of a typical flotation cell. The froth is assumed to be incompressible and therefore streamlines for the flow pattern can be calculated as constant values of the stream function ψ which satisfies the Laplace equation

$$\frac{\partial^2 \psi}{\partial x^2} + \frac{\partial^2 \psi}{\partial y^2} = 0 \qquad (9.66)$$

subject to suitable boundary conditions. Because there is almost no macroscale turbulence in the froth, the streamlines represent the path taken by a bubble through the froth. Streamlines that terminate on the top surface of the froth represent bubbles that burst on the surface while streamlines that terminate on the vertical plane above the overflow weir represent bubbles that pass into the concentrate stream. It is not difficult to calculate the streamline trajectories for simple froth geometries such as those shown in Figures 9.15 and 9.16 because solutions to the Laplace equation for these geometries are readily available. Carslaw and Jaeger (1959) is a good source for these solutions. It is necessary only to specify the boundary conditions for the particular cell geometry that is to be studied.

The boundary conditions are formulated in terms of the gas flows across the various boundaries of the froth. The gas flow across the pulp-froth interface is related to the aeration rate in the flotation cell G m^3/s. Consider a flotation cell with a rectangular cross-section and a side-to-side dimension w meters and a front-to-back dimension b meters. The superficial gas velocity through the pulp-froth interface is $\frac{G}{wb}$ and the linear aeration rate is $\frac{G}{w}$ per unit length of interface. The total gas flow through the interface that is bounded by the back wall of the cell and an imaginary line a distance x from the back wall is $\frac{Gx}{b}$. Thus, if the value of the stream function against the back wall is given the reference value 0, the value of the stream function at a distance x from the back wall is $\psi = \frac{Gx}{b}$. The stream function can be normalized as

$$\Psi = \frac{\psi}{G} \qquad (9.67)$$

and Ψ also obviously satisfies equation 9.66. The dimensions of the froth are normalized with respect to the cell dimension b.

$$x' = \frac{x}{b}$$
$$y' = \frac{y}{b} \qquad (9.68)$$

On the pulp-froth interface the boundary value for the stream function Ψ is given by $\Psi = x'$.

Similarly the stream function is zero along the entire back wall because no air passes through that plane. No gas passes through the front wall beneath the overflow weir. An important feature of the pattern of streamlines in the froth is the fractional split of the gas flow between that contained in the concentrate froth and that which leaves the froth through the top surface where bubbles burst and release gas. If a fraction 1 - α of the froth passes over the weir, the streamline that passes through the top right hand corner of the froth is associated with the stream function with normalized value α because this streamline separates the recovered froth from the froth that terminates its life by bursting on the top surface. Thus the boundary condition along the top surface of the froth is

$$\Psi = \alpha x' \qquad (9.69)$$

and along the front wall

$$\Psi = 1 \qquad \text{for } 0 < y \leq Wh \qquad (9.70)$$

and

$$\Psi = 1 - (1 - \alpha)\frac{y - Wh}{H - Wh} \qquad \text{for } Wh < y < H \qquad (9.71)$$

where H represents the total height of the froth layer and Wh represents the height of the weir above the pulp-froth interface.

The parameter α is determined largely by the stability of the froth. Stable froths tend to rise higher above the pulp thus forcing more froth over the weir into the concentrate. Unstable froth tend to break more easily and consequently more gas leaves the froth through the top surface. Lower values of α represent more stable froths. Obviously the mobility of the froth also affects the value of parameter α since greater mobility of the froth phase will allow more to be recovered over the weir.

Carslaw and Jaeger provide a convenient steady state solution to equation 9.66 in a rectangular region with three sides having $\Psi = 0$ and an arbitrary function along the fourth side. The solution to the present problem can be obtained by superimposing three separate solutions each with the appropriate boundary function specified for the pulp-froth interface, the top surface of the froth or the front wall and concentrate overflow.

The general solution has the form

$$\Psi(x',y') = \Psi_1(x',y') + \Psi_2(1-x',H'-y') + \Psi_3(y',1-x') \qquad (9.72)$$

where

$$\Psi_i(x',y') = \sum_{n=1}^{\infty} a_n^{(i)} \sin n\pi x' \frac{1 - \exp(-2n\pi(H' - y'))}{1 - \exp(-2n\pi H')} \exp(-n\pi y') \tag{9.73}$$

represents the solution for boundary *i* and the coefficients $a_n^{(i)}$ for each solution are given by

$$\begin{aligned} a_n^{(1)} &= -\frac{2}{n\pi}(-1)^n && \text{(pulp–froth interface)} \\ a_n^{(2)} &= \frac{2\alpha}{n\pi} && \text{(upper surface of froth)} \\ a_n^{(3)} &= \frac{2}{n\pi}\left(1 - \alpha(-1)^n + \frac{1-\alpha}{n\pi(1 - Wh')}\sin(n\pi Wh')\right) && \text{(front edge)} \end{aligned} \tag{9.74}$$

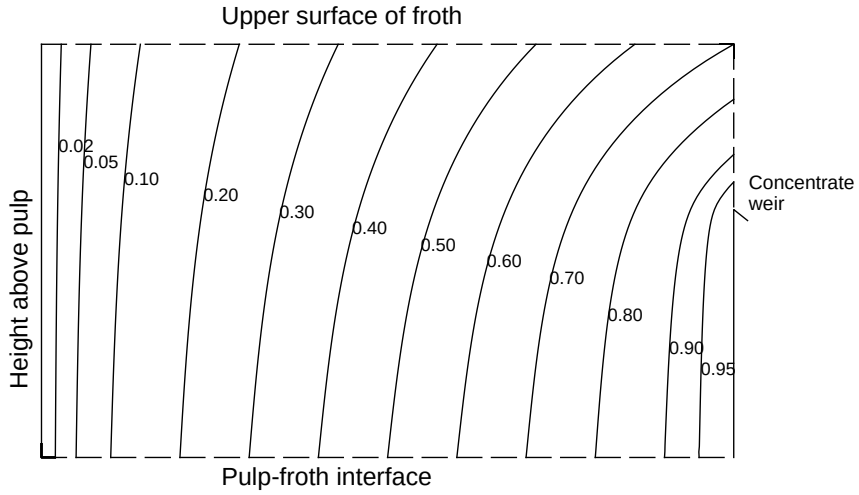

Figure 9.15 *Streamlines in flotation froth calculated from equation 9.72. The froth is relatively unstable with stability coefficient 1 - α = 0.7. Solid boundary lines are impermeable to air which can flow only through boundaries represented by broken lines.*

The contours for constant values of Ψ (the streamlines) calculated from equation 9.72 are illustrated in Figures 9.15 and 9.16 These figures give a visual picture of the flow of the froth.

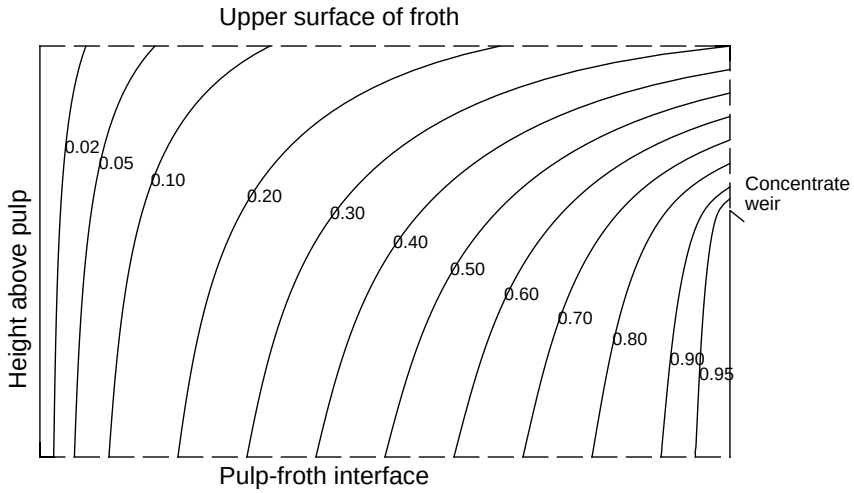

Figure 9.16 *Streamlines in flotation froth calculated from equation 9.72. The froth is relatively stable with stability coefficient 1 - α = 0.3. Solid boundary lines are impermeable to air which can flow only through boundaries represented by broken lines.*

8.7.2 Dynamic Processes in the Froth Phase

As individual bubbles in the froth move upward towards the free surface and laterally toward the overflow weir, a number of dynamic processes occur. The most obvious of these is the coarsening of the froth structure due to rupture of the lamellar films between the bubbles. A rupture of this kind gives rise to a sudden increase in the bubble volume and the froth structure becomes increasingly coarse. This phenomenon is easily observable on any flotation cell and there are a number of studies underway aimed at diagnosing the behavior of the froth from the size of bubbles in the top layer which can be measured fairly easily by image analysis techniques.

The rupturing of a film in the froth leads to the partial detachment of the hydrophobic particles that were present in the film before rupture. The water and particles contained in the ruptured lamellar film are transferred to the plateau borders that are connected to the film. It is reasonable to suppose that some of the particles will, however, remain attached at the air-water interface and will simply move to a neighboring lamellar film. Particles that have a high hydrophobicity (high contact angle) will have a greater tendency to remain attached while particles with lower hydrophobicity will tend to transfer to the Plateau borders. This is the origin of the upgrading that can occur in the froth, a phenomenon that has been observed in experiments.

The water in the Plateau borders together with its load of suspended solids drains under gravity through the network of Plateau borders so the froth becomes steadily denuded of both water and particles as it moves toward the overflow weir.

Hydrophilic particles that entered the froth by entrainment are unlikely to become attached to bubbles in the froth and they are free to drain from the froth with the water. Particles also settle relative to the water because of their greater density and this adds to the downward flux of particles in the Plateau borders.

Particles that are entrained in the water in the lamellar films that separate the bubbles do not drain from the lamellar films to the Plateau borders because they are hindered by other particles that are attached to the bubble surfaces. This restriction was first suggested by Gaudin who provided a sketch to illustrate the idea.

The rate of breakage of lamellar films is governed in a complex fashion by the surface tension of the fluid, the concentration and type of surfactants, the thickness of the film, the presence of particles, particularly those having high contact angles, the differential pressure across the film and the size of the bubble, and therefore the area, of the film. Dippenaar (1982) has demonstrated that hydrophobic particles with high contact angles lead to fairly rapid film rupture but there is also evidence that hydrophobic particles with lower contact angles have a stabilizing effect on the froth. This can sometimes be observed in flotation plants where the froth produced in cleaner cells are often more stable than those produced in rougher or scavenger cells.

The dynamic behavior of the froth and its evolution with time is governed by three rate processes: the rate of drainage of water from the lamellar film into the Plateau borders, the rate of breakage of the lamellar films, and the rate of drainage of water and suspended solids from the Plateau borders. In addition, the compositions of the particle populations in the lamellar films and the Plateau borders at any point in the froth phase are governed by the differential rate of detachment of the different types of particle from the lamellar films into the Plateau borders.

These individual rate processes are difficult to observe and study in the laboratory so that almost no reliable information is currently available on appropriate model structures that can be used for their description in quantitative terms. It is however useful to formulate a simple model for each process and to superimpose these on the model of the froth motion that is described in Section 9.7.1 This leads to an overall kinetic model for the flotation process that captures the elements of the all important subprocesses that occur in the froth and which is capable of calibration against operating data. This model for the froth phase can be combined with the kinetic models for the pulp phase to generate a viable model structure that can be used for simulation of operating flotation cells and flotation plants.

8.7.3 Rate of breakage of lamellar films

The rate of breakage of the lamellar films that separate bubbles in the froth is a complex process that depends on many factors. The two internal properties of the froth that are most directly affected by the rupturing of the lamellar films are the surface area per unit volume of froth and the amount and composition of the solids that remain attached to the bubble surfaces. The amount of water and solid and the composition of the solid in the Plateau borders is also determined by the film breakage

process because each rupture event adds both water and, selectively, solid particles to the Plateau borders.

The rate at which lamellar films break varies throughout the froth layer but the factors that determine the rate of breakage are not well enough understood at the present time to attempt anything but the simplest simulation of this subprocess and its effect on the performance of the flotation cell. Accordingly a simple model for the breakage of lamellar films is used here. A method is now developed to calculate amount and composition of the solid concentrate and the amount of water that is recovered over the weir.

The method of solution is based on the observation that individual bubbles pass through the froth entirely on a single streamline. Thus the dynamic changes that occur during the time that a bubble is in the froth can be evaluated by integration along a streamline. This can be illustrated by calculating bubble surface area per unit volume of froth from the time that a bubble enters the froth until it leaves in the concentrate or bursts on the surface of the froth. Let S_F represent bubble surface area per unit volume of froth. A differential balance on the surface area in the froth gives

$$u_x \frac{\partial S_F}{\partial x} + u_y \frac{\partial S_F}{\partial y} = -R_B \tag{9.75}$$

where u_x and u_y are the local components of the froth motion and R_B is the rate of breakage of lamellar films per unit volume of froth. The incompressibility of the froth requires

$$\frac{\partial u_x}{\partial x} + \frac{\partial u_y}{\partial y} = 0 \tag{9.76}$$

The solution to equation 9.75 can be generated by integrating along a streamline since all streamlines are characteristic lines for this equation. The local components of the velocity vector can be obtained by differentiation of the stream function.

$$u_x = \frac{1}{w}\frac{\partial \psi}{\partial y} = \frac{G}{wb}\frac{\partial \Psi}{\partial y'} = \frac{G}{wb}u_x' = U_G u_x' \tag{9.77}$$

and

$$u_y = -\frac{1}{w}\frac{\partial \psi}{\partial x} = -\frac{G}{wb}\frac{\partial \Psi}{\partial x'} = \frac{G}{wb}u_y' = U_G u_y' \tag{9.78}$$

where $U_G = \frac{G}{wb}$ is the superficial gas velocity across the pulp-froth interface.

Along a streamline

$$\frac{dS_F}{dy} = -\frac{R_B}{u_y} \tag{9.79}$$

which is easy to integrate numerically starting at $S_F = \frac{6}{D_b}$ at $y = 0$. D_b is the diameter of the bubble

as it leaves the pulp phase. It is convenient to normalize S_F with respect to the surface area per unit volume of a single spherical bubble as it emerges from the pulp phase and R_B with respect to the surface area production rate in the flotation cell $\frac{6G}{D_b}$

$$S_F' = S_F \frac{D_b}{6} \tag{9.80}$$

$$R_B' = R_B \frac{D_b wb^2}{6G} \tag{9.81}$$

Then equation 9.79 becomes

$$\frac{dS_F'}{dy'} = -\frac{R_B'}{u_y'} \tag{9.82}$$

with $S_F' = 1$ at $y' = 0$.

Each bubble burst alters the amount of solid that is attached to the bubble surfaces that bound the lamellar films because there is a strong tendency for the attached solid to become detached and to enter the water in the Plateau borders as suspended solid. Not all of the adhering solid will become detached and some will remain attached at the air-water interface and will slide along the surface and join the attached load on a neighboring lamellar film. This phenomenon is described by a solid attachment coefficient σ_{ij} which is the fraction of particles of type *ij* that remain attached during a bursting event. σ_{ij} depends strongly on the size and hydrophobicity of the particle. Highly hydrophobic particles have a greater tendency to remain attached and this is the primary mechanism by which the grade of mineral increases in the froth as the froth moves up from the pulp surface. This phenomenon has been observed in practice and is sometimes exploited to improve the grade of the concentrate in industrial flotation cells. The composition of the solid attached to bubble surfaces is governed by the equation

$$u_x \frac{\partial S_F \Gamma_{ij}}{\partial x} + u_y \frac{\partial S_F \Gamma_{ij}}{\partial y} = -(1 - \sigma_{ij}) \Gamma_{ij} R_B \tag{9.83}$$

where Γ_{ij} is the amount of solid of type *ij* attached per unit area of bubble surface. σ_{ij} is the fraction of type *ij* that remains attached during the rupture of a single lamellar film. The streamlines are characteristics for equation 9.83 and along a streamline

$$\frac{dS_F \Gamma_{ij}}{dy} = -\frac{(1 - \sigma_{ij}) \Gamma_{ij} R_B}{u_y} \tag{9.84}$$

which must be integrated from the initial condition $\Gamma_{ij} = m_{ij} LL_{max}$ at $y = 0$. LL_{max} is the load carried by the bubbles when they leave the pulp phase and m_{ij} is the mass fraction of particles of type *ij* in the bubble load. Γ_{ij} is normalized by

$$\Gamma_{ij}' = \frac{\Gamma_{ij}}{m_{ij} L L_{\max}} \tag{9.85}$$

and equation 9.84 is normalized

$$\frac{d\Gamma_{ij}'}{dy'} = \sigma_{ij} \frac{\Gamma_{ij}' R_B'}{S_F' u_y'} \tag{9.86}$$

S_F' and Γ_{ij}' can be calculated along a characteristic streamline using equation 9.82 and equation 9.86 provided that a model for bubble bursting rate can be formulated. The rate at which laminar films rupture is assumed here to be constant.

The residence time of any bubble in the froth is obtained by integrating along a streamline

$$\frac{d\tau'}{dy'} = \frac{1}{u_y'} \tag{9.87}$$

where τ' is the bubble residence time normalized with respect to the superficial velocity of the gas.

$$\tau' = \frac{\tau U_G}{b} \tag{9.88}$$

Equations 9.82 and 9.86 can be integrated to simultaneously to give explicit expressions for S_F' and Γ_{ij}' throughout the froth in terms of the residence time as a parameter.

$$S_F' = 1 - R_B' \tau' \tag{9.89}$$

$$\Gamma_{ij}' = \left(S_F'\right)^{-\sigma_{ij}} = \left(1 - R_B' \tau'\right)^{-\sigma_{ij}} \tag{9.90}$$

These expressions are necessary for calculating the conditions in the network of Plateau borders throughout the froth as descibed in Section 9.7.4.

8.7.4 **Froth Drainage through Plateau Borders**

Flow of slurry in the network of Plateau borders varies throughout the froth. The rate at which water and solids drain through the network is larger at the bottom of the froth because of the accumulated water and solids due to breakage of lamellar films as the froth flows toward the surface or the concentrate weir. The water and solids that drains from the lamellar films and which leaves the films because of the breakage mechanism that is described in Section 9.7.3 causes a steady increase in the flow through the Plateau borders which increase in cross-sectional area to accommodate the additional flow. The slurry that drains through the Plateau borders is driven by gravity and consequently moves relative to the moving froth.

The path that any element of draining slurry takes through the froth can be calculated from the streamlines established for the froth and therefore for the network of Plateau borders which moves integrally with the froth. The velocity at which the slurry drains relative to the network can be approximated by assuming laminar flow under gravity in the Plateau borders. A short segment of a channel within the network of Plateau borders might appear as shown in Figure 9.17. In a channel inclined at angle θ to the vertical the average velocity relative to the channel wall is

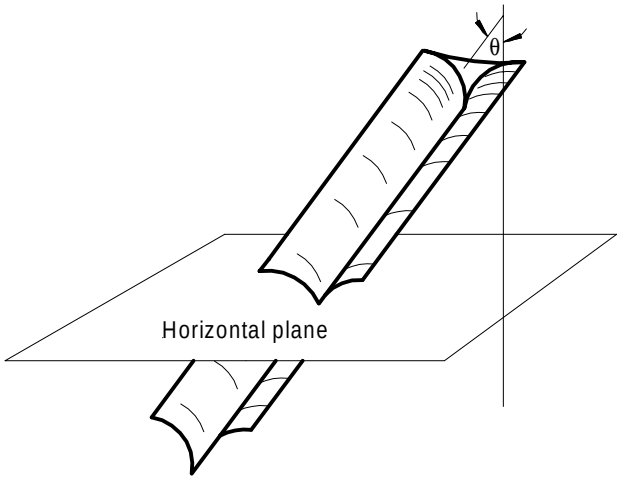

Figure 9.17 *Segment in the network of Plateau borders through which the slurry drains under gravity.*

$$V(\theta) = \frac{g\rho\cos\theta D_H^2}{32\mu} \qquad (9.91)$$

where D_H is the hydraulic diameter of the channel. The Plateau borders are assumed to have no preferred orientation so that θ is uniformly distributed in the interval [0, π/2]. The average draining velocity is

$$\begin{aligned} \bar{V} &= \frac{2}{\pi}\int_0^{\pi/2} \frac{g\rho D_H^2}{16\pi\mu} d\theta \\ &= \frac{g\rho D_H^2}{16\pi\mu} \end{aligned} \qquad (9.92)$$

If D_H remains constant throughout the froth, $\bar{V}$ may be taken as constant and the components of the vector of draining water velocities in the froth is

$$\begin{aligned} v_x &= u_x \\ v_y &= u_y - \bar{V} \end{aligned} \qquad (9.93)$$

The characteristic trajectories for draining slurry are defined by

$$\frac{dx}{dy} = \frac{v_x}{v_y} = \frac{u_x}{u_y - \bar{V}} \qquad (9.94)$$

which are integrated starting at $y = H$.

For convenience, equation 9.94 can be written in terms of normalized variables

$$\frac{dx'}{dy'} = \frac{u_x'}{u_y' - \bar{V}'} \qquad (9.95)$$

where

$$\bar{V}' = \frac{\bar{V}}{U_g} \tag{9.96}$$

A typical set of trajectories calculated from equation 9.95 are shown in Figure 9.16. Trajectories that pass over the concentrate weir represent water and solids that are recovered by entrainment. Those trajectories that end on the pulp-froth interface represent slurry that is returned from the froth to the pulp phase.

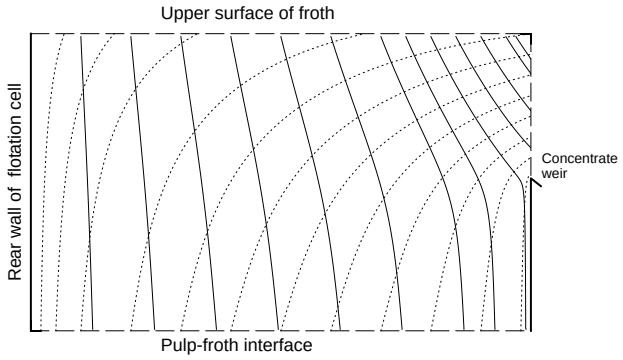

Figure 9.18 *Drainage trajectories for slurry in the network of Plateau borders.*

The quantity of slurry that drains through the network of Plateau borders increases steadily from the top of the froth because the bursting bubbles continually add water to the drainage channels which become increasingly larger in cross-section to accommodate the increase in the rate of drainage. If ε represents the volume of the Plateau borders per unit volume of froth, the differential volume balance for the draining slurry is

$$u_x \frac{\partial \varepsilon}{\partial x} + (u_y - \bar{V}) \frac{\partial \varepsilon}{\partial y} = \frac{1}{2} R_B \delta \tag{9.97}$$

where δ is the average thickness of the lamellar films in the froth. Equation 9.97 must be solved with boundary conditions specified along the top surface of the froth which reflect the release of slurry due to the bursting of the bubbles on that surface. All lamellar films break that are associated with the gas that escapes through the top surface of the froth and the slurry produced enters the Plateau borders and starts to drain down the network of channels. Any wash water that is added to the top surface of the froth also adds to the flow at the upper surface.

$$\begin{aligned} \bar{V}\varepsilon &= \frac{1}{2} S_F \delta \alpha U_G + \text{wash water rate} \qquad \text{at } y = H \\ \varepsilon &= 3 \frac{S_F' \delta' \alpha}{\bar{V}'} + \frac{\text{wash water rate}}{\bar{V}} \end{aligned} \tag{9.98}$$

The drainage trajectories shown in Figure 9.18 are characteristic lines for the solution of equation 9.97. Along any trajectory

$$\frac{d\varepsilon}{dy} = \frac{1}{2} \frac{R_B \delta}{u_y - \bar{V}} \tag{9.99}$$

In terms of normalized variables

$$\frac{d\varepsilon}{dy'} = \frac{3R_B'\delta'}{u_y' - \bar{V}'} \tag{9.100}$$

where $\delta' = \frac{\delta}{D_b}$.

A differential balance for the concentration C_{ij} of solids of type *ij* in the slurry in the Plateau borders is

$$u_x\frac{\partial \varepsilon C_{ij}}{\partial x} + (u_y - \bar{V} - v_{Tij})\frac{\partial \varepsilon C_{ij}}{\partial y} = (1 - \sigma_{ij})R_B\Gamma_{ij} \tag{9.101}$$

where v_{Tij} is the terminal settling velocity in the narrow channels of particles of type *ij*
Boundary conditions are

$$C_{ij} = \frac{2\Gamma_{ij}}{\delta} \qquad \text{at } y = H \tag{9.102}$$

Characteristic lines for this equation can be calculated by integrating

$$\frac{dx'}{dy'} = \frac{u_x'}{u_y' - \bar{V}' - \frac{v_{Tij}}{U_G}} \tag{9.103}$$

These lines have the same general shape as the drainage characteristics but are somewhat steeper becoming almost vertical throughout most of the froth for particles that settle rapidly.

Along these characteristic lines

$$\frac{d\varepsilon C_{ij}}{dy} = \frac{(1 - \sigma_{ij})R_B\Gamma_{ij}}{u_y - \bar{V} - v_{Tij}} \tag{9.104}$$

In terms of normalized variables

$$\frac{d\varepsilon C_{ij}'}{dy'} = \frac{(1 - \sigma_{ij})R_B'\Gamma_{ij}'}{u_y' - \bar{V}' - \frac{v_{Tij}}{U_G}} \tag{9.105}$$

with

$$C_{ij}' = \frac{C_{ij}D_b}{6m_{ij}LL_{\max}} \tag{9.106}$$

Equation 9.105 Must be solved after the surface concentration Γ_{ij} has been evaluated at every point in the froth by solution of equation 9.86.

The total concentration of particles of type *ij* in a sample drawn from any point in the froth is given by

$$\text{Froth sample concentration} = \varepsilon C_{ij} + S_F \Gamma_{ij} \qquad \text{kg/m}^3 \tag{9.107}$$

Samples can be drawn from different points in the froth on operating cells and compared with the model predictions using this equation.

It is now possible to evaluate the fractional recovery of particles of type *ij* by the froth. This quantity is called the froth transmission coefficient γ_{ij} and it is an important link between the pulp phase kinetics and the recovery of solids. Its use in a simulation model is discussed in Section 9.8.1. The froth transmission coefficient can be evaluated by integrating the flow of particles, both those attached to lamellar films and those entrained in the Plateau borders, in the streams that pass across the concentrate weir.

$$\begin{aligned} \gamma_{ij} &= \frac{w\int_{Wh}^{H}(u_x S_F \Gamma_{ij})_{x=b}\,dy + w\int_{Wh}^{H}(u_x \varepsilon C_{ij})_{x=b}\,dy}{\frac{6}{D_b} g m_{ij} L L_{\max}} \\ &= \int_{Wh'}^{H'} u_x'(S_F' \Gamma_{ij}' + \varepsilon C_{ij}')_{x'=1}\,dy' \end{aligned} \tag{9.108}$$

Likewise, the recovery of water to the concentrate stream can be calculated from

$$\frac{Q_w^C}{G} = \int_{Wh'}^{H'} u_x'(3 S_F' \delta' + \varepsilon)\,dy' \tag{9.109}$$

The calculated values of the froth transmission coefficient using equation 9.108 are shown as a function of the retention coefficient σ_{ij} and the stability factor for the froth in Figure 9.19. The flowrate of water over the concentrate weir calculated from equation 9.109 is given in Table 9.1

Table 9.1 Calculated values of the recovery of water through the froth phase.

Stability coefficient 1- α = 0.7		Stability coefficient 1 - α = 0.2	
Breakage rate *RB* m^2/m^3 s	Concentrate water flow m^3 water/m^3 air	Breakage rate R_B m^2/m^3 s	Concentrate water flow m^3 water/m^3 air
0.0	0.0326	0.0	0.0279
0.2	0.0292	0.5	0.0200
0.4	0.0259	0.7	0.0168
0.6	0.0225	0.9	0.0137

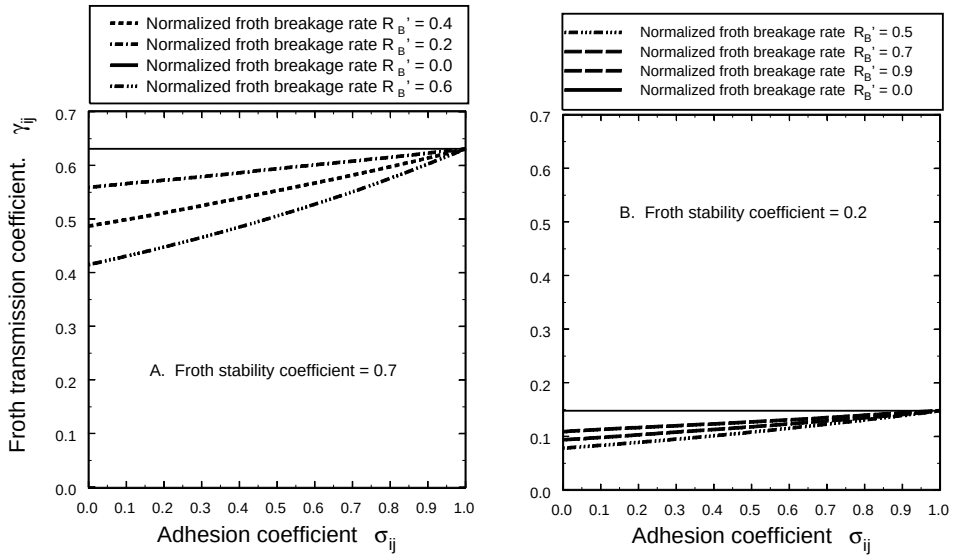

Figure 9.19 *Froth transmission coefficient calculated using equation 9.108 for a flotation froth having a weir height equal to 51.4% of the total froth height. A. Relatively stable froth with α = 0.3 and B. relatively unstable froth with α = 0.8.*

The data in Figure 9.19 B shows that the value of the froth transmission coefficient can be quite small if the froth is not stable. These low values of γ_{ij} have often been observed in industrial flotation cells. The application of the froth transmission coefficient is described in Section 9.8.1. The froth transmission coefficient has an upper limit that is determined by the froth stability and the relative height of the weir. In practice the froth stability can be controlled by the nature and concentration of frother and the weir height can be varied by control of the pulp level in the flotation cell. These are control actions that are often exploited in industrial practice.

8.8 Simplified Kinetic Models for Flotation

Many batch flotation tests that have been conducted in the laboratory have indicated that the kinetic model for flotation does describe the essential nature of the flotation process at least in a well stirred flotation environment where the solid particles are kept in suspension and are available for capture by the bubbles. The analysis presented in Section 9.2 indicates that the rate at which particles are captured on to the bubble surfaces is proportional to the concentration of the particles in the pulp phase. Particles of different type will have different specific capture rates primarily because of the variation of floatability due to variation in the contact angle exhibited by the particle surfaces. There is abundant evidence in the literature that the particle size also influences the rate of capture of particles. This is reflected in the model for the specific flotation constant K_{ij} that is described in Section 9.3 which leads to equations 9.32 and 9.33 for the rate of transfer of particles from the pulp phase to the bubble phase.

$$\text{Rate of transfer of particles of type } ij = K_{ij}C_{ij} = \kappa_{ij}SC_{ij} \qquad (9.110)$$

In this equation the indices refer to the particle size and particle composition type respectively. K_{ij} and κ_{ij} are complex functions of the particle size, bubble size, bubble loading and of the attachment induction time which is apparently dominated by the contact angle that is exhibited by a particle in the environment of the flotation cell.

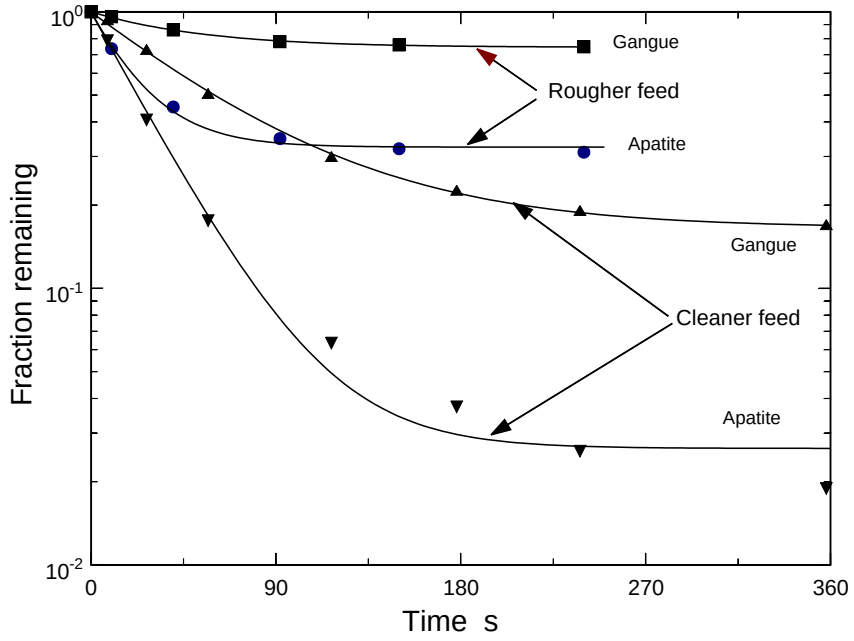

Figure 9.20 *Typical results of batch flotation tests. Data from King (1978)*

Many experimental studies, particularly in laboratory batch flotation cells, have shown that it is unusual to find K_{ij} or κ_{ij} to be constant in a single test. This is illustrated in Figure 9.20 where the fraction of mineral remaining as a function of time in a batch flotation test is shown. The mineral apatite was essentially completely liberated from the gangue minerals in this experiment so particles of mixed composition are not a significant factor in this case.

The batch test is described by

$$\frac{dC_{ij}}{dt} = -K_{ij}C_{ij} \qquad (9.111)$$

which integrates to

$$\frac{C_{ij}(t)}{C_{ij}(0)} = \exp(-K_{ij}t) \qquad (9.112)$$

If the process were governed entirely by equation 9.111 the data in Figure 9.20 would plot as a straight line according to equation 9.112. It clearly does not and the specific rate of flotation of both minerals has decreased during the course of the test and both eventually stop floating. This kind of behavior can be described by assuming that a fraction of each mineral is non floatable and has $K_{ij} = 0$. This fraction is related to the ultimate recovery by $\mathcal{R}_{ij}$ and equation 9.112 becomes

$$\begin{aligned} \frac{C_{ij}(t)}{C_{ij}(0)} &= \Re_{ij}\exp(-K_{ij}t) + (1 - \Re_{ij}) \\ &= 1 - \Re_{ij}(1 - \exp(-K_{ij}t) \end{aligned} \tag{9.113}$$

This is often written in terms of the recovery, R_{ij}, of the mineral species

$$R_{ij} = \frac{C_{ij}(0) - C_{ij}(t)}{C_{ij}(0)} = \Re_{ij}\left(1 - \exp(-K_{ij}t)\right) \tag{9.114}$$

If both K_{ij} and $\mathcal{R}_{ij}$ in equation 9.114 are regarded as adjustable parameters, this simple model can be made to fit the data well as can be seen for the data collected from the rougher feed in Figure 9.20. The lines on the graph show the best fit of equation 9.114 to the data. Many such sets of data collected from a wide range of batch flotation cells can be found in the literature.

There are a number of issues raised by data such as that shown in Figure 9.20. Firstly the feed material had quite a broad size distribution as shown in Figure 9.21. The analysis presented in Section 9.2 shows that the collision and attachment probabilities, and therefore the specific flotation rate constant, are functions of the particle size. The curvature in Figure 9.20 could be due to the effect of the particle size distribution. This could occur because the particles having sizes favorable for flotation will float relatively rapidly leaving the slower floating sizes in the pulp with the consequent steady decline in the average specific rate of flotation. In fact this is the cause of the apparent lack of fit to the simple model shown for the cleaner feed. Another possible explanation for the steady decline in the specific rate of flotation is the possibility that the froth phase progressively loses its ability to transmit to the overflow lip the particles that are attached to bubbles. Factors such as a steady decline in frother concentration during the test contribute to this phenomenon which is often observed as a steady decline in the froth collection rate during the course of a batch flotation test.

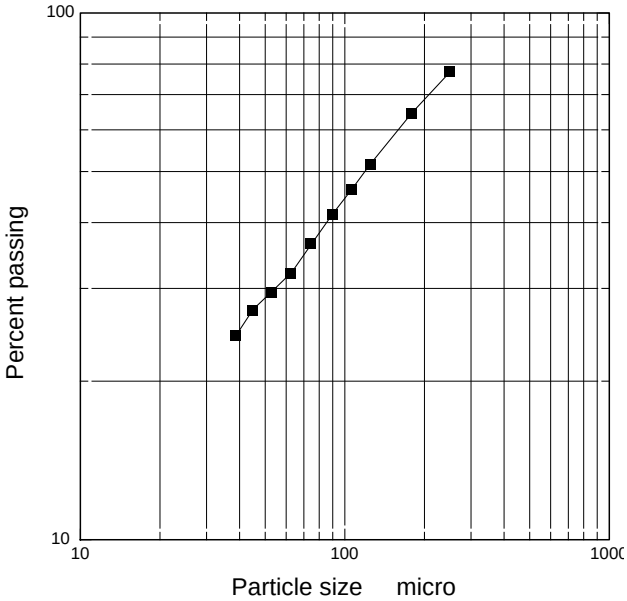

Figure 9.21 *Particle size distribution of material tested in Figure 9.20*

Some authors, notably Imaizumi and Inoue (1965), have postulated that the rate constant is

distributed over a broad continuum of values. In practice this has rarely been found to be an effective model for describing actual flotation data mostly because the continuous distribution would have to be bimodal with a definite concentration around the value 0 representing the non-floatable components.

The differences exhibited by the two experiments shown in Figure 9.20 is instructive. The data labeled rougher feed represents the raw flotation feed produced by milling. The data labeled cleaner feed shows the results of floating the accumulated concentrate from the rougher float. It is immediately obvious that the non floatable component for both the mineral and the gangue is reduced considerably in the cleaner feed. In the case of apatite it is reduced to about 2%. This is consistent with the postulate that non-floatable material should never get into the concentrate. Any small amount in the rougher concentrate can be attributed to entrainment.

If this simple kinetic model is to be useful for practical application to real flotation systems, the effect of varying particle size must be included. A simple approach that has proved to be effective in allowing for the effect of particle size is to split the specific flotation rate constant K_{ij} into three factors using equation 9.33 as a guide

$$K_{ij} = k_j \Phi_j(d_{pi}) S_{av} \tag{9.115}$$

$\Phi_j(d_{pi})$ includes all the effects of particle size but it can also depend on the particle type. S_{av} is the available bubble surface area averaged over the entire bubble population in the flotation cell. k_j is a residual constant that is specific to the particle type and is independent of particle size.

The average available surface area S_{av} can be modeled using a method proposed by Pogorely (1962) who noted that the rate at which the available surface area on a bubble decreases can be modeled by equation 9.49

$$V_c A \frac{dS}{d\tau} = MAS \sum_j k_j \Phi_j(d_{pi}) p_{ij} = MAS\bar{k} \tag{9.116}$$

where M is the mass of solids in the cell and p_{ij} is the fraction of the solids in the cell that is in composition class j and size class i. V_c is the volume of the flotation cell and A is the bubble surface area per unit volume.

The available surface area after the bubble has been in the cell for a time τ is obtained by integration of equation 9.116

$$\begin{aligned} S &= \exp\left(-\frac{M\tau}{V_c} \sum_j k_j \Phi_j(d_{pi}) p_{ij} \right) \\ &= \exp\left(-\frac{M\tau\bar{k}}{V_c} \right) \end{aligned} \tag{9.117}$$

The average available area in the cell is obtained by averaging S over the interval from 0 to τ_b where τ_b is the time that a bubble spends in the cell.

$$S_{av} = \int_0^{\tau_b} S d\tau = \frac{V_c}{M\tau_b \bar{k}}\left(1 - \exp\left(-\frac{M\tau_b \bar{k}}{V_c}\right)\right) \tag{9.118}$$

8.8.1 **Application to Flotation Cells in Complex Flowsheets**

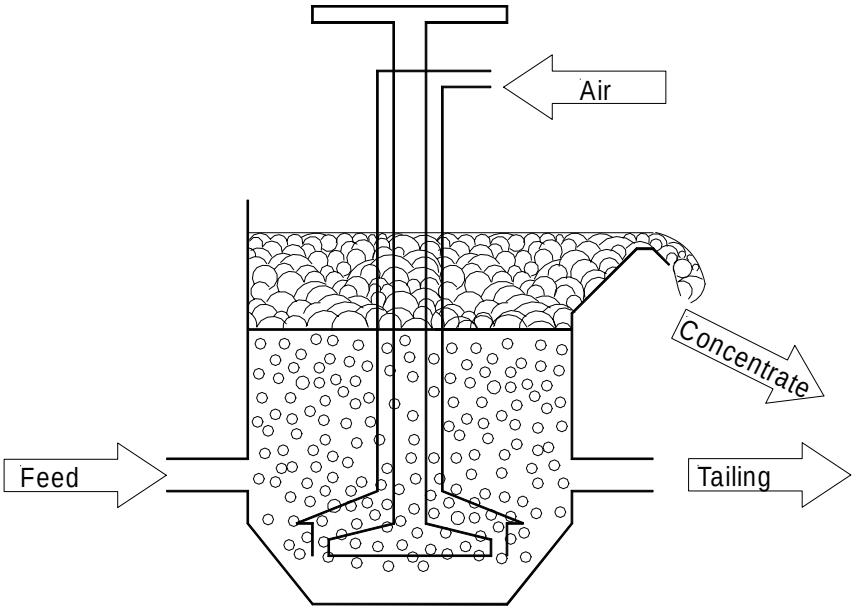

Figure 9.22 *Schematic of a continuous well-mixed flotation cell.*

The rate of transfer of particles of type *ij* to the froth phase in a perfectly mixed flotation cell is

$$\text{Rate of transfer} = k_j \Phi_j(d_{pi}) S_{av} M p_{ij} \qquad \text{kg/s} \tag{9.119}$$

A material balance for particles of type *ij* is

$$\begin{aligned} W^F p_{ij}^F &= W^C p_{ij}^C + W^T p_{ij}^T \\ &= \gamma_{ij} k_j \Phi_j(d_{pi}) S_{av} M p_{ij}^T + W^T p_{ij}^T \end{aligned} \tag{9.120}$$

where γ_{ij} is the froth transmission coefficient for particles of type *ij*.

$$W^T p_{ij}^T = \frac{W^F p_{ij}^F}{1 + \gamma_{ij} k_j \Phi(d_{pi}) S_{av} \dfrac{M}{W^T}} \tag{9.121}$$

The residence time of the solids in the cell is based on the flowrate of tailings

$$\theta_T = \frac{M}{W^T} \tag{9.122}$$

which is usually approximated as

$$\theta_T = \frac{V_p}{Q^T} \tag{9.123}$$

where V_p is the volume of pulp in the cell and Q_T is the volumetric flowrate of the tailing stream equal to the sum of the water and solids volumetric flowrates.

$$\begin{aligned} Q^T &= Q_s^T + Q_w^T \\ &= \sum_{ijk} \frac{Wp_{ij}^T}{\rho_{sj}} + Q_w^T \end{aligned} \tag{9.124}$$

Where ρ_{sj} is the density of the solid in composition class *j*.
Equation 9.121 becomes

$$W^T p_{ij}^T = \frac{W^F p_{ij}^F}{1 + \gamma_{ij} k_j \Phi(d_{pi}) S_{av} \theta_T} \tag{9.125}$$

which is the working equation used to simulate the operation of a single continuous flotation cell. This equation requires iterative solution because both S_{av} and θ_T depend on the solution p_{ij}^T through equations 9.118, 9.123, 9.124 and 9.125.

In practice each particle type has more than one associated specific rate constant. Usually there are two – one for the floatable fraction and one, equal to zero, for the non-floatable fraction. Occasionally, more than two rate constants are associated with a particular type although this is unusual in practice. The discrete distribution of particle types is accordingly extended into a third dimension and we write p_{ijk} to represent the fraction of the particle population in size class *i*, composition class *j*, and flotation rate class *k*. There is a unique value of the specific rate constant *k* associated with each *k* class. When applying the model to a complete flotation circuit, it is postulated that any particles that enter the plant in flotation rate class *k* will remain in that class throughout their sojourn in the plant. It is possible that the value of the flotation rate constant that is associated with a specific *k* class will change its value at a specific point in the plant. For example the addition of collector at the head of a scavenger or cleaner bank will usually lead to an increase in the value of the rate constant for that bank of cells.

8.8.2 **The effect of particle size on the rate of flotation**

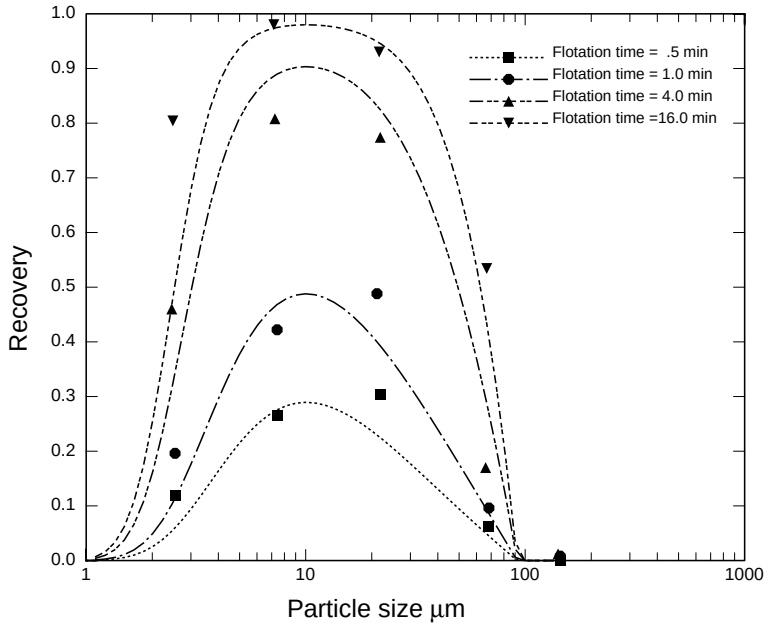

Figure 9.23 *Recovery of galena in a batch flotation cell as a function of particle size. Data from Trahar (1976). Lines are calculated using equation 9.127*

The function $\Phi_j(d_{pi})$ that is introduced into equation 9.115 must account for the effects of particle size on the collision, attachment and detachment probabilities. A number of empirical expressions appear in the literature for the separate probabilities and a composite function that attempts to account for all three simultaneously is given by

$$\Phi_j(d_{pi}) = 2.33\left(\frac{\varepsilon}{d_{pi}^2}\right)^{½}\exp\left(-\frac{\varepsilon}{d_{pi}^2}\right)\left(1 - \left(\frac{d_{pi}}{d_{p\max}}\right)^{1.5}\right) \qquad (9.126)$$

This equation has two constants ε and $d_{p\,max}$. ε is related to the level of turbulence in the flotation pulp and $d_{p\,max}$ is the size of the largest particle that can be floated without detachment from the bubble. Although the theoretical foundation for this equation is only approximate, it has been found to be reasonably successful in describing the measured dependence of the flotation rate constant on particle size. The parameters in equation 9.126 can be estimated from recovery-by-size data collect from a simple batch flotation test. Substituting K_{ij} from equation 9.115 into equation 9.112 gives

$$R_{ij} = 1 - \exp\left(-k_j S_{av}\Phi_j(d_{pi})t\right) \qquad (9.127)$$

A typical set of data for galena is shown in Figure 9.23. The lines on the graph were calculated using equation 9.127 with ε = 112 µm^2 and $d_{p\,max}$ = 92 µm. In spite of the scatter in the measured data, the variation of recovery with particle size is reasonably well represented by equation 9.127.

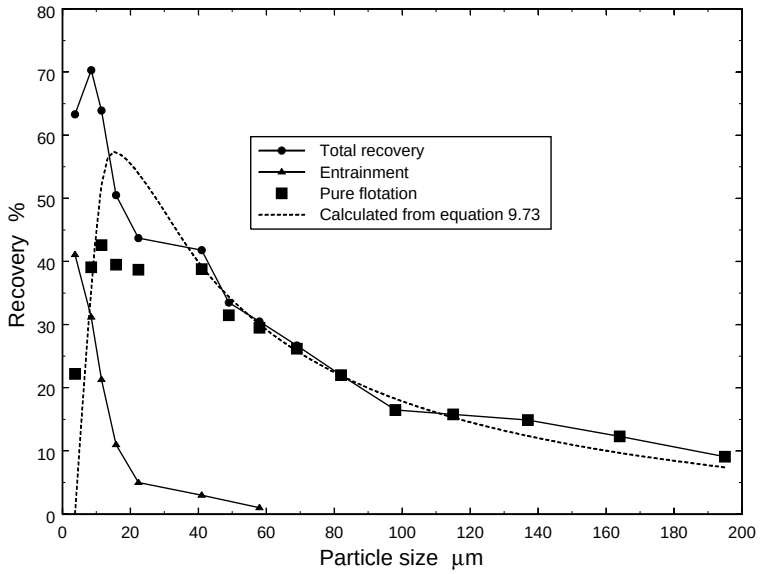

Figure 9.24 *recovery of cassiterite as a function of particle size measured in a batch flotation cell. Data from de Ruiter (1979). The broken line was calculated using equation 9.127.*

The measured recovery at very fine sizes should be corrected for the effects of entrainment which can account for a substantial fraction of the recovered particles at these sizes. This correction can be easily made for minerals that have no natural floatability. A blank test is run without collector so that all the recovery is due to entrainment. An example is shown in Figure 9.24. The measured entrained recovery was subtracted from the total recovery to generate the true flotation recovery which is represented by square symbols in the figure. The true flotation recovery is compared to that calculated from equation 9.127 in the figure. The function $\Phi_j(d_{pi})$ given by equation 9.126 with ε = 130 μm^2 and $d_{p\,max}$ = 400 μm fits the data well.

The parameter ε in equation 9.126 is comparatively easy to estimate because it is related directly to the particle size, $d_{p\,m}$ at which the recovery is a maximum through the equation

$$\varepsilon = 0.5 d_{p\,m}^2 \qquad (9.128)$$

The constant 2.33 in equation 9.126 normalizes the function so that $\Phi_j(d_{p\,m}) = 1.0$.

8.8.3 **The Water Balance in an Operating Flotation Cell**

The water balance across the flotation cell can be established in a number of ways. The rate of water transfer by bubbles into the froth phase together with a model for froth breakage and drainage is the most reliable model for this purpose but the model described in Section 9.7 has not yet been developed to the stage where the parameters can be related for prediction purposes to the

thermodynamic properties of the flotation environment. However the stability coefficient 1-α, the froth breakage rate R_B and the lamellar film thickness δ can be estimated from measurements of the water recovery rate at different froth heights. Two alternative methods have been found to be useful in practice: the total solids content of either the concentrate or tailings stream can be specified.

If the solid content of the concentrate, s^C, is specified the calculation of the water balance is straightforward once equation 9.125 has been solved. The volumetric flowrate of water in the concentrate is

$$Q_w^C = \frac{1 - s^C}{\rho_w s^C} \sum_{ijk} W^C p_{ijk}^C \tag{9.129}$$

where ρ_w is the density of the water. From equation 9.119

$$Q_w^C = \frac{1 - s^C}{\rho_w s^C} \sum_{ijk} \gamma_{ij} k_j \Phi_j(d_{pi}) S_{av} \theta^T W^T p_{ijk}^T \tag{9.130}$$

The water flow in the tailing stream is obtained by difference

$$Q_w^T = Q_w^F - Q_w^C \tag{9.131}$$

If the solid content, s^T, of the tailing stream is specified

$$Q_w^T = \frac{1 - s^T}{\rho_w s^T} \sum_{ijk} W^T p_{ijk}^T \tag{9.132}$$

and the water flowrate in the concentrate stream is obtained by difference.

$$Q_w^C = Q_w^F - Q_w^T \tag{9.133}$$

8.9 Symbols Used in this Chapter

b Distance from front to back of flotation cell, m.
C_{ij} Concentration of particles of type *ij* in the pulp or in the slurry entrained in the froth, kg/m^3.
C_D Drag coefficient of a rising bubble.
D_{be} Volume equivalent bubble diameter, m.
D_{bh} Horizontal projection of bubble diameter, m.
d_{pi} Particle size in class *i*, m.
$d_{p\,max}$ Largest particle that can remain attached to a bubble, m.
E_{Aij} Attachment efficiency for particles of type *ij*.
E_{Cij} Collision efficiency for particles of type *ij*.
E_{Dij} Detachment efficiency for particles of type *ij*.
$\mathscr{F}$ Function that defines the effect of the radial coordinate on the stream line around a rising bubble.
$F_{\theta c}$ Distribution of particle collision angles.

$f_{\theta c}$ Distribution density for particle collision angles.
$F_{ij}(t_{ind})$ Distribution of induction times for particles of type *ij*.
$f_{ij}(t_{ind})$ Distribution density for induction times for particles of type *ij*.
G Aeration rate in a flotation cell, m^3/s.
G_v Specific aeration rate in flotation cell per unit volume of cell. s^{-1}.
g_j Particle grade in grade class *j*.
K_{ij} Specific flotation rate constant for particles of type *ij*. s^{-1}.
L Fraction of bubble surface that is covered by adhering particles.
L_{max} Load carried by completely covered bubble.
Q_s Volumetric flowrate of solid, m^3/s.
Q_w Volumetric flowrate of water, m^3/s.
r Radial coordinate, m.
r' $\frac{r}{R_b}$
r_p' $\frac{R_p}{R_b}$
R_b Radius of bubble, m.
R_B Bubble bursting rate in the froth.
R_p Radius of particle, m.
R_o Distance from collision centerline far in front of bubble, m.
R_{oij} R_o for particle of type *ij* having a grazing trajectory, m.
Re_b Bubble Reynolds number.
$\Re_{Ij}$ Ultimate recovery of particles of type *ij*.
S_{av} Average available bubble surface area per unit volume of cell, m^{-1}.
S_F Bubble surface area per unit volume of froth, m^{-1}.
S_v Surface area of bubble per unit volume of cell, m^{-1}.
t_{ind} Induction time, s.
t_s Sliding time, s.
$\overline{t}_{ind}$ Average of the induction time distribution, s.
u Velocity vector, m/s.
U_b Rise velocity of bubble, m/s.
U_G Superficial velocity of gas through the pulp-froth interface, m/s.
v Velocity vector, m/s.
v_{Tij} Terminal settling velocity of particles of type *ij*, m/s.
$\overline{V}$ Average velocity of draining slurry relative to the froth, m/s.
W Mass flowrate of solid, kg/s.
Wh Weir height, m.
x' Normalized vertical coordinate in the froth, *x/b*.
y' Normalized vertical coordinate in the froth, *y/b*.

α Parameter
α_{ij} Parameter for distribution of induction time for particles of type *ij*.

β_{ij} Parameter for distribution of induction time for particles of type *ij*.
γ_{ij} Froth transmission coefficient.
Γ_{ij} Concentration of particles of type *ij* attached to bubble surface in the froth, kg/m^2.
δ Thickness of lamellar film in froth, m.
η_{ij} Packing density for particles of type *ij* on bubble surface, kg/m^3.
θ Polar coordinate.
θ_c Collision angle.
θ_L Loading angle
θ_p Angle subtended by particle radius when particle touches the bubble surface.
θ_T residence time of pulp in flotation cell, s.
κ Specific flotation rate constant, m/s.
μ_w Viscosity of water, Pa s.
ρ_w Density of water, kg/m^3.
σ Variance of induction time distribution, s^2.
σ_{ij} Fraction of particles of type *ij* that remain attached to bubble surface during a bubble burst event in the froth.
τ Residence time in the froth measured along a froth streamline, s.
Φ Dimensionless number $C_D Re^2_{bh}$.
$\Phi(d_p)$ Function to describe the variation of flotation rate constant with particle size.
Ψ Normalized stream function.
ψ Stream function.

8.10 Bibliography

The fundamental basis of the collision model for flotation kinetics is due to Sutherland (1948) and is discussed in detail in Sutherland and Wark (1955). This model has been widely discussed in the literature and many researchers have contributed to its development. Some of the key ideas are developed in Flint and Howarth(1971), Reay and Ratcliffe (1973) and Yoon and Luttrell (1989) and the work of these authors forms the basis of the model for collision efficiency that is presented here. Many of the hydrodynamic considerations of bubble motion are discussed in Clift *et al.*(1978). Schulze(1983) has presented a comprehensive analysis of many aspects of the model.

The model for the rise velocity of bubbles is based on the analysis of Karamanev and Nikolov (1992) and Karamanev (1994). Data on measured bubble rise velocities is given by Allen (1900), Fuerstenau and Wayman (1958) and Afruns and Kitchener (1976).

Tomlinson and Fleming (1965) investigated experimentally the effect of bubble loading on the rate of flotation and described its effects. Measured data on bubble loading is given by King *et al.* (1974) and Bradshaw and O'Connor (1996)

The distributed kinetic constant model has been widely discussed and used because laboratory batch experiments can almost invariably be described using the concept. The first formal statement that

mineral particles showed the peculiar behavior of possessing a non floatable component appears to be due to Morris (1952).

The effect of particle size on the flotation recovery is reviewed by Trahar and Warren (1976). The model for particle detachment was based on the presentation of Drzymala (1994).

Questions relating to the conditioning of the surfaces of the common types of minerals that are treated by flotation are discussed in King (1982). Some quantitative results are presented but the information is largely qualitative and therefore not directly applicable to model calculations and simulation.

The potential flow model for the froth phase is due to Moys (1978, 1984). Moys (1989) and Cutting (1989) have summarized measurements that have been made by taking samples from the froth of operating flotation cells. The model of the froth behavior presented here is based on Murphy *et al.* (1996), Neethling and Cilliers (1999) and Neethling *et al.* (2000) who have investigated the behavior of froths using experimental and simulation techniques. Their methods produce models of the behavior of the froth phase that are significantly more realistic than the simple model that is used here.

The discrete distributed flotation model originated with Zaidenberg *et al.* in 1964. The application of this model to the simulation of flotation plants is based on King (1973, 1975) and Sutherland (1977)

8.11 **References**

Afruns, J. P. and Kitchener, J. A. (1976) The absolute rate of capture of single particles by single bubbles. Flotation. Gaudin Memorial Volume. M. C. Fuerstenau Editor. SME pp625-637.

Allen, H. S. (1900) The motion of a sphere in a viscous fluid. *Philosophical Magazine* Vol. 50 pp.323-338.

Bradshaw, D. J. and O'Connor, C. T. (1996) Measurement of the sub-process of bubble loading in flotation. *Minerals Engineering.* Vol. 9 pp. 443-448.

Clift, R., Grace, J. R. and Weber, M.. E. (1978). Bubbles, Drops and Particles. Academic Press.

Cutting, G. W. (1989) Effect of froth structure and mobility on plant performance. *Mineral Processing and Extractive Metallurgy Review.* Vol. 5, pp 169-201.

de Ruiter, M. A.(1979) Particle size effects in the flotation of cassiterite. Msc. Thesis University of the Witwatersrand, Johannesburg,

Drzymala, J. (1994) Characterization of materials by Hallimond tube flotation. Part 2: maximum size of floating particles and contact angle. *Intl. Jnl. Mineral Processing* Vol 42, pp 153-168

Flint, L. R. and Howarth, W. J. (1971) The collision efficiency of small particles with spherical air bubbles. *Chemical Engineering Science*. Vol 26, pp. 115-1168.

Fuerstenau, D. W. and Wayman, C. H.(1958) Effect of chemical reagents on the motion of single air bubbles in water. *Trans. AIME* Vol. 211 pp. 694-699.

Imaizumi, T. and Inuoe, T. (1965) Kinetic considerations of froth flotation. *Proc. 6th Intl. Mineral Processing Congress*. A. Roberts Editor, Pergamon Press. Oxford

Karamanev, D. G.(1994) Rise of gas bubbles in quiescent liquids. *AIChE Journal* Vol. 40 pp.1418-1421.

Karamanev, D. G. and Nikolov, L. N. (1992) Free rising spheres do not obey Newton's Law for free settling. *AIChE Journal* Vol. 38 pp.1843-1846.

King, R. P. (1973). Model for the design and control of flotation plants. Applications of Computer Methods in the Mineral Industry. Eds. M. D. G. Salamon and F. H. Lancaster. S. Afr. Inst. Min. Metall. Johannesburg. Pp. 341-350.

King, R. P. (1975). Simulation of flotation plants. *Trans. AIME.* Vol. 258, pp.286-293

King, R. P. (1978) A pilot-plant investigation of a kinetic model for flotation. *Jnl. South African Inst. Min. Metall.* Vol 78. Pp. 325-338.

King, R. P.(1982) Editor, Principles of Flotation. S. Afr. Inst. Min. Metall. Johannesburg..

King R. P., Hatton, T. A. and Hulbert, D. G. (1974) Bubble loading during flotation. *Trans. Instn. Min. Metall*. Vol C. pp.C112-C115.

Morris, T. M.(1952) Measurement and Evaluation of the rate of flotation as a function of particle size. *Trans. AIME.* Vol. 193. pp.794-797.

Moys. M. H. (1978) A study of a plug flow model for flotation froth behavior. *Intl. Jnl. Mineral Processing.* Vol 5. pp21-38.

Moys, M. H. (1984) Residence time distribution and mass transport in the froth phase of the flotation process. *Intl. Jnl. Mineral Processing.* Vol 13. pp117-142.

Moys, M. H. (1989) Mass transport in flotation froths. *Mineral Processing and Extractive Metallurgy Review.* Vol. 5, pp 203-228.

Murphy, D. G., Zimmerman, W. and Woodburn, E. T. (1996). Kinematic model of bubble motion in a flotatio froth. *Powder Technology.* Vol. 87, pp 3-12.

Neethling, S. J. and Cilliers, J. J. (1999) A visual kinematic model of flowing foams incorporating coalescence. *Powder Technology.* Vol. 101 249-256.

Neethling, S. J., Cilliers, J. J. and Woodburn, E. T. (2000) Prediction of the water distribution in a flowing foam. *Chem. Engng. Science.* Vol 55. Pp. 4021-4028.

Neethling, S. J. and Cilliers, J. J. (2000) A model for free solids motion in froths. Private communication.

Pogorely, A. D. (1962) Limits of the use of the kinetic equation proposed by K F Beloglazov. *Izv. Vuz. Tsvetnaya Metaurgia.* No 1 pp. 33-40. Available in English as NIM-TR-158 from Mintek. Randburg. S. Africa

Reay, D. and Ratcliffe, G. A. (1973). Removal of fine particles from water by dispersed air floatation: effect of bubble size and particle size on collision efficiency. *Canadian Journal of Chemical Engineering* Vol. 51, pp. 178-185.

Schulze, H. J. (1993) Physico-chemical Elementary Processes in Flotation. Elsevier, Amsterdam.

Sutherland, D. N. (1977) An appreciation of galena concentration using a steady-state flotation model. *Intl. Jnl. Mineral Processing*. Vol. 4 pp. 149-162.

Sutherland K. L. (1948) Physical chemistry of flotation XI. Kinetics of the flotation process. *Jnl. Physical Chemistry.* Vol. 52 pp. 394-425.

Sutherland K. L. and Wark, I. W. (1955) Principles of Flotation. Australasian Institute of Mining and Metallurgy. Melbourne.

Tomlinson, H. S. and Fleming, M. G. (1965) Flotation rate studies. Proc. 6th International Mineral Processing Congress. A. Roberts Editor. Pergamon Press.

Trahar W. J. (1976) The selective flotation of galena from sphalerite with special reference to the effects of particle size. *Intl. Jnl. Mineral Processing*. Vol 3 pp. 151-166

Trahar W. J. and Warren, L. J. (1976) The floatability of very fine particles – A review. *Intl. Jnl. Mineral processing.* Vol 3 pp.103-131.

Yoon, R. H. and Luttrell, G. H. (1989) The effect of bubble size on fine particle flotation. *Mineral Processing and Extractive Metallurgy Review*. Vol 5. pp. 101-122.

Zaidenberg, I. Sh. Lisovskii, D. I. And Burovoi, I. A. (1964) One approach to the construction of a mathematical model for flotation processes. *Soviet Journal of Non-ferrous Metals*. English translation Vol. 5. pp. 26-32.